

Euclid preparation. Using mock Low Surface Brightness dwarf galaxies to probe Wide Survey detection capabilities

Euclid Collaboration: M. Urbano^{★1}, P.-A. Duc¹, M. Poulain², A. A. Nucita^{3,4,5}, A. Venhola², O. Marchal¹, M. Kümmel⁶, H. Kong⁷, F. Soldano⁸, E. Romelli⁹, M. Walmsley^{10,11}, T. Saifollahi¹, K. Voggel¹, A. Lançon¹, F. R. Marleau¹², E. Sola¹³, L. K. Hunt¹⁴, J. Junais^{15,16}, D. Carollo⁹, P. M. Sanchez-Alarcon^{15,16}, M. Baes¹⁷, F. Buitrago^{18,19,20}, Michele Cantiello²¹, J.-C. Cuillandre²², H. Domínguez Sánchez²³, A. Ferré-Mateu^{15,16}, A. Franco^{4,3,5}, J. Gracia-Carpio²⁴, R. Habas²¹, M. Hilker²⁵, E. Iodice²⁶, J. H. Knapen^{15,16}, M. N. Le^{15,16}, D. Martínez-Delgado²⁷, O. Müller^{28,13,29}, F. De Paolis^{3,4,5}, P. Papaderos³⁰, R. Ragusa²⁶, J. Román³¹, E. Saremi³², V. Testa³³, B. Altieri³⁴, L. Amendola³⁵, S. Andreon³⁶, N. Auricchio³⁷, C. Baccigalupi^{38,9,39,40}, M. Baldi^{41,37,42}, S. Bardelli³⁷, P. Battaglia³⁷, A. Biviano^{9,38}, E. Branchini^{43,44,36}, M. Brescia^{45,26}, S. Camera^{46,47,48}, G. Cañas-Herrera^{49,50}, V. Capobianco⁴⁸, C. Carbone⁵¹, J. Carretero^{52,53}, S. Casas⁵⁴, M. Castellano³³, G. Castignani³⁷, S. Cavuoti^{26,55}, A. Cimatti⁵⁶, C. Colodro-Conde¹⁵, G. Congedo⁵⁷, C. J. Conselice¹¹, L. Conversi^{58,34}, Y. Copin⁵⁹, F. Courbin^{60,61}, H. M. Courtois⁶², M. Cropper⁶³, A. Da Silva^{64,65}, H. Degaudenzi⁶⁶, G. De Lucia⁹, H. Dole⁶⁷, F. Dubath⁶⁶, C. A. J. Duncan⁵⁷, X. Dupac³⁴, S. Dusini⁶⁸, S. Escoffier⁶⁹, M. Farina⁷⁰, R. Farinelli³⁷, S. Ferriol⁵⁹, F. Finelli^{37,71}, M. Frailis⁹, E. Franceschi³⁷, M. Fumana⁵¹, S. Galeotta⁹, K. George⁷², B. Gillis⁵⁷, C. Giocoli^{37,42}, A. Grazian⁷³, F. Grupp^{24,6}, L. Guzzo^{74,36,75}, S. V. H. Haugan⁷⁶, W. Holmes⁷⁷, I. M. Hook⁷⁸, F. Hormuth⁷⁹, A. Hornstrup^{80,81}, K. Jahnke⁸², M. Jhabvala⁸³, B. Joachimi⁸⁴, E. Keihänen⁸⁵, S. Kermiche⁶⁹, A. Kiessling⁷⁷, B. Kubik⁵⁹, M. Kunz⁸⁶, H. Kurki-Suonio^{87,88}, R. Laureijs⁸⁹, A. M. C. Le Brun⁹⁰, S. Ligi⁴⁸, P. B. Lilje⁷⁶, V. Lindholm^{87,88}, I. Lloro⁹¹, G. Mainetti⁹², D. Maino^{74,51,75}, E. Maiorano³⁷, O. Mansutti⁹, O. Marggraf⁹³, M. Martinelli^{33,94}, N. Martinet⁹⁵, F. Marulli^{96,37,42}, R. J. Massey⁹⁷, E. Medinaceli³⁷, S. Mei^{98,99}, Y. Mellier^{100,8}, M. Meneghetti^{37,42}, E. Merlin³³, G. Meylan²⁸, A. Mora¹⁰¹, M. Moresco^{96,37}, L. Moscardini^{96,37,42}, R. Nakajima⁹³, C. Neissner^{7,53}, S.-M. Niemi⁴⁹, C. Padilla⁷, S. Paltani⁶⁶, F. Pasian⁹, K. Pedersen¹⁰², V. Pettorino⁴⁹, S. Pires²², G. Polenta¹⁰³, M. Poncet¹⁰⁴, L. A. Popa¹⁰⁵, L. Pozzetti³⁷, F. Raison²⁴, R. Rebolo^{15,106,16}, A. Renzi^{107,68}, J. Rhodes⁷⁷, G. Riccio²⁶, M. Roncarelli³⁷, R. Saglia^{6,24}, Z. Sakr^{35,108,109}, D. Sapone¹¹⁰, B. Sartoris^{6,9}, P. Schneider⁹³, T. Schrabback¹², A. Secroun⁶⁹, G. Seidel⁸², S. Serrano^{111,112,113}, P. Simon⁹³, C. Sirignano^{107,68}, G. Sirri⁴², L. Stanco⁶⁸, J.-L. Starck²², J. Steinwagner²⁴, P. Tallada-Crespí^{52,53}, A. N. Taylor⁵⁷, H. I. Teplitz¹¹⁴, I. Tereno^{64,20}, N. Tessore⁸⁴, S. Toft^{115,116}, R. Toledo-Moreo¹¹⁷, F. Torradeflot^{53,52}, I. Tutusaus^{113,111,108}, L. Valenziano^{37,71}, J. Valiviita^{87,88}, T. Vassallo^{9,72}, G. Verdoes Kleijn⁸⁹, A. Veropalumbo^{36,44,43}, Y. Wang¹¹⁴, J. Weller^{6,24}, G. Zamorani³⁷, I. A. Zinchenko¹¹⁸, E. Zucca³⁷, M. Ballardini^{119,120,37}, M. Bolzonella³⁷, E. Bozzo⁶⁶, C. Burigana^{121,71}, R. Cabanac¹⁰⁸, A. Cappi^{37,122}, D. Di Ferdinando⁴², J. A. Escartin Vigo²⁴, L. Gabarra¹²³, M. Huertas-Company^{15,124,125,126}, J. Martín-Fleitas¹²⁷, S. Matthew⁵⁷, N. Mauri^{56,42}, R. B. Metcalf^{96,37}, A. Pezzotta³⁶, M. Pöntinen⁸⁷, C. Porciani⁹³, I. Risso^{36,44}, V. Scottez^{100,128}, M. Sereno^{37,42}, M. Tenti⁴², M. Viel^{38,9,40,39,129}, M. Wiesmann⁷⁶, Y. Akrami^{130,131}, I. T. Andika^{132,133}, S. Anselmi^{68,107,134}, M. Archidiacono^{74,75}, F. Atrio-Barandela¹³⁵, D. Bertacca^{107,73,68}, M. Bethermin¹, A. Blanchard¹⁰⁸, L. Blot^{136,90}, M. Bonici^{137,51}, S. Borgani^{138,38,9,39,129}, M. L. Brown¹¹, S. Bruton¹³⁹, A. Calabro³³, B. Camacho Quevedo^{38,40,9}, F. Caro³³, C. S. Carvalho²⁰, T. Castro^{9,39,38,129}, F. Cogato^{96,37}, S. Conseil⁵⁹, A. R. Cooray¹⁴⁰, O. Cucciati³⁷, S. Davini⁴⁴, G. Desprez⁸⁹, A. Díaz-Sánchez¹⁴¹, J. J. Díaz¹⁵, S. Di Domizio^{43,44}, J. M. Diego²³, M. Y. Elkhassab^{9,39,138,38}, A. Enia^{37,41}, Y. Fang⁶, A. G. Ferrari⁴², A. Finoguenov⁸⁷, K. Ganga⁹⁸, J. García-Bellido¹³⁰, T. Gasparetto³³, V. Gautard¹⁴², E. Gaztanaga^{113,111,143}, F. Giacomini⁴², F. Gianotti³⁷, G. Gozaliasl^{144,87}, M. Guidi^{41,37}, C. M. Gutierrez¹⁴⁵, A. Hall⁵⁷, H. Hildebrandt¹⁴⁶, J. Hjorth¹⁰², J. J. E. Kajava^{147,148}, Y. Kang⁶⁶, V. Kansal^{149,150}, D. Karagiannis^{119,151}, K. Kiiveri⁸⁵, J. Kim¹²³, C. C. Kirkpatrick⁸⁵, S. Kruk³⁴, J. Le Graet⁶⁹, L. Legrand^{152,153}, M. Lembo^{8,119,120}, F. Lepori¹⁵⁴, G. Leroy^{155,97}, G. F. Lesci^{96,37}, J. Lesgourgues⁵⁴, L. Leuzzi³⁷, T. I. Liaudat¹⁵⁶, A. Loureiro^{157,158}, J. Macias-Perez¹⁵⁹, G. Maggio⁹, M. Magliocchetti⁷⁰, F. Mannucci¹⁴, R. Maoli^{160,33}, C. J. A. P. Martins^{161,30}, L. Maurin⁶⁷, M. Miluzio^{34,162}, P. Monaco^{138,9,39,38,129}, C. Moretti^{9,38,39,40}, G. Morgante³⁷, K. Naidoo^{143,84}, A. Navarro-Alsina⁹³, S. Nesseris¹³⁰, D. Paoletti^{37,71}, F. Passalacqua^{107,68}, K. Paterson⁸², L. Patrizii⁴², A. Pisani⁶⁹, D. Potter¹⁵⁴, S. Quai^{96,37}, M. Radovich⁷³, G. Rodighiero^{107,73}, S. Sacquogna^{21,3,4}, M. Sahlén¹⁶³, D. B. Sanders¹⁶⁴, E. Sarpa^{40,129,39}, A. Schneider¹⁵⁴, D. Sciotti^{33,94}, E. Sellentin^{165,50}, L. C. Smith¹³, J. G. Sorce^{166,67}, K. Tanidis¹²³, C. Tao⁶⁹, G. Testera⁴⁴, R. Teyssier¹⁶⁷, S. Tosi^{43,44,36}, A. Troja^{107,68}, M. Tucci⁶⁶, C. Valieri⁴², D. Vergani³⁷, G. Verza¹⁶⁸, P. Vielzeuf⁶⁹, and N. A. Walton¹³

September 17, 2025

ABSTRACT

Local Universe dwarf galaxies are both cosmological and mass assembly probes. Deep surveys have enabled the study of these objects down to the low surface brightness (LSB) regime. In this paper, we estimate *Euclid*'s dwarf detection capabilities as well as limits of its MERge processing function (MER pipeline), responsible for producing the stacked mosaics and final catalogues. To do this, we inject mock dwarf galaxies in a real Euclid Wide Survey (EWS) field in the VIS band and compare the input catalogue to the final MER catalogue. The mock dwarf galaxies are generated with simple Sérsic models and structural parameters extracted from observed dwarf galaxy property catalogues. To characterize the detected dwarfs, we use the mean surface brightness inside the effective radius SB_e (in mag arcsec^{-2}). The final MER catalogues achieve completenesses of 91 % for $SB_e \in [21, 24]$, and 54 % for $SB_e \in [24, 28]$. These numbers do not take into account possible contaminants, including confusion with background galaxies at the location of the dwarfs. After taking into account those effects, they become respectively 86 % and 38 %. The MER pipeline performs a final local background subtraction with small mesh size, leading to a flux loss for galaxies with $R_e > 10''$. By using the final MER mosaics and reinjecting this local background, we obtain an image in which we recover reliable photometric properties for objects under the arcminute scale. This background-reinjected product is thus suitable for the study of Local Universe dwarf galaxies. *Euclid*'s data reduction pipeline serves as a test bed for other deep surveys, particularly regarding background subtraction methods, a key issue in LSB science.

Key words. Galaxies: dwarf – Techniques: image processing – Catalogues

1. Introduction

The Λ CDM standard model suggests that galaxies originate from the first small, low-mass haloes that were formed as a result of primordial variations in the density of cold dark matter (e.g., Dekel & Silk 1986). Today, we observe a diverse range of galaxies in the Local Universe, varying in size, mass, and morphology. In particular, galaxies at the low-mass end, known as dwarf galaxies, can exhibit a low surface brightness (LSB), and come in a variety of morphologies. Local Universe dwarf galaxies can also be used as cosmological probes whose number and distribution around larger galaxies constrain dark matter models in simulations (e.g., Spergel & Steinhardt 2000; Bode et al. 2001; Kopolov et al. 2009; Nadler et al. 2019).

The detection and identification of dwarf galaxies have encountered significant challenges. Over the past decades, wide surveys such as SDSS (Abazajian et al. 2003, 2005) and Pan-STARRS (Chambers et al. 2016), and deep Andromeda galaxy surveys such as PHAT (Dalcanton et al. 2012) and PANDAS (McConnachie et al. 2009; Doliva-Dolinsky et al. 2022, 2023), have extended the list of the known dwarf satellites of the Local Group to fainter luminosities, and helped map their distribution. Technological advancements in terms of sensitivity in astronomical camera systems have unveiled LSB diffuse stellar features, extending the study of dwarf galaxies from the Local Group to much further in the Local Universe, where galaxies cannot be resolved into individual stars anymore.

Several projects have extended the study of dwarfs to larger distances, such as the surveys conducted by the Canada-France-Hawaii telescope (including MATLAS: Habas et al. 2020; Marleau et al. 2021; Poulain et al. 2021; Heesters et al. 2023, CFIS: Ibata et al. 2017, NGVS: Ferrarese et al. 2012), the Survey Telescope of the Very Large Telescope VST (including the Fornax Deep Survey, e.g., Venhola et al. 2018), the Subaru telescope (e.g., Aihara et al. 2017; Kaviraj et al. 2025), and the Dark Energy Spectroscopic Instrument (including SMUDGes: Zaritsky et al. 2019), as well as the Dragonfly Telephoto Array (e.g., Abraham & van Dokkum 2014). In addition to camera sensitivity, the detection of these diffuse stellar structures faces another technical challenge: the preservation of the LSB signal throughout the image processing pipelines. In particular, sub-optimal lo-

cal background subtraction leads to an extremely problematic loss of flux, especially in the case of extended, faint objects. The aforementioned projects have therefore had to resort to the development of dedicated pipelines optimised for the preservation of LSB signal (for instance, Elixir-LSB: Ferrarese et al. 2012; Duc et al. 2015), whose development remains central for future surveys (e.g., Euclid Collaboration: Borlaff et al. 2022; Kelvin et al. 2023).

The European Space Agency's *Euclid* space telescope (Euclid Collaboration: Mellier et al. 2025) will pioneer the observation of large portions of the sky from space. During its Early Release Observations (using the ERO LSB-optimised pipeline, Cuillandre et al. 2025a) and its first quick data release (Q1, Euclid Collaboration: Aussel et al. 2025), *Euclid* proved to be an efficient LSB machine, allowing teams to detect stellar structures down to the LSB regime (Cuillandre et al. 2025b), dwarf galaxies and their nuclei (Marleau et al. 2025; Euclid Collaboration: Marleau et al. 2025), intracluster light (ICL, e.g., Euclid Collaboration: Bellhouse et al. 2025) and its globular clusters in the Perseus and Fornax clusters (Kluge et al. 2025; Saifollahi et al. 2025b), as well as tidal features in Dorado group galaxies (Urbano et al. 2025). Those studies could be extended to the Euclid Wide Survey (EWS, Euclid Collaboration: Scaramella et al. 2022) provided its pipeline, different from that of the ERO, preserves the LSB signal.

This paper aims to assess the performance of the EWS in detecting Local Universe LSB objects, focusing on dwarf galaxies, including ultra-diffuse and LSB galaxies, as case studies. We use SB_e the mean surface brightness inside the effective radius R_e , defined as

$$SB_e = I_E + 2.5 \log_{10}(2\pi R_e^2) \quad (1)$$

in mag arcsec^{-2} , with I_E the total apparent magnitude of the dwarf in the VIS band and R_e in arcsec, for a galaxy with an axis ratio of $b/a = 1$.

We focus on results of source injection in optical *Euclid* images. The structure of the article is as follows: Sect. 2 presents the data utilised in this study and details our methods for injecting dwarfs, and the parameters studied. The detection capabilities and limits are presented in Sect. 3, followed by a discussion in Sect. 4. Finally, the conclusions are summarised in Sect. 5.

* e-mail: mathias.urbano@gmail.com

2. Data and methods

In this section, we present the *Euclid* data and the chosen approach for injecting dwarfs into them. In particular, we give relevant details about the EWS merge processing function (referred to as the MER pipeline), whose main outputs are the MER mosaics constructed from stacked exposures and the final MER catalogues. Given the overwhelming amount of image data to be handled, studies such as the search for dwarf galaxies across the full extent of the EWS will rely on selection criteria applied to the final MER catalogue (e.g. [Euclid Collaboration: Marleau et al. 2025](#)). In this section, we detail the method we used to assess the performance of this product.

2.1. *Euclid* images and MER catalogues

2.1.1. Definition of the dataset

The *Euclid* space telescope operates with a visible and a near-infrared instrument. This article focuses on the visible imager (VIS, [Cropper et al. 2016](#); [Euclid Collaboration: Cropper et al. 2025](#)) that uses the optical I_E filter with a detector composed of $6 \times 6 = 36$ CCDs (i.e. $4 \times 36 = 144$ quadrants), covering 0.57 deg^2 with a pixel scale of $0''.1$.

In the EWS data processing, the captured raw images are processed by the *Euclid* Science Ground Segment (SGS) standard pipelines. The first step is the calibration through the VIS pipeline ([Euclid Collaboration: McCracken et al. 2025](#)). The output are calibrated single exposure data cubes (which include debiased and flat-fielded images, flag maps, and noise maps). There are also separate files for weights and background maps generated using the NoiseChisel tool from GNU Astronomy Utilities (Gnuastro, [Akhlaghi & Ichikawa 2015](#); [Akhlaghi 2019](#)), intended for use in exposure co-addition. This co-addition is performed by SWarp ([Bertin et al. 2002](#)) in a second pipeline, MER ([Euclid Collaboration: Romelli et al. 2025](#)), which creates 0.25 deg^2 mosaics¹ from stacked images, subtracts the VIS background, calculates and subtracts an additional local background, and produces the source catalogues using SourceExtractor++ ([Bertin et al. 2020](#); [Euclid Collaboration: Borlaff et al. 2022](#)). Typically, each patch of the sky is covered by four long and two short VIS single calibrated exposures of a *Euclid* Reference Observation Sequence (ROS). A mosaic can require more exposures to be fully covered, since depending on its location, a tile can cover areas of several observations.

Since the start of EWS data acquisition, SGS pipeline products² have been distributed on-the-fly to the Euclid Consortium through the ESA Science Archive. From those data, we extract a set of 16 EWS calibrated single exposures in I_E that suffice to produce one complete MER mosaic. The chosen MER tile (see Appendix A) is centred on $RA = 2^\circ 35' 43''.41$, $Dec = -51^\circ 30' 0''.00$ or $l = 271.148^\circ$, $b = -58.706^\circ$. It corresponds to an expected background level of approximately $22 \text{ mag arcsec}^{-2}$

¹ In other works, such an image is often referred to as a tile. Here, however, we follow the *Euclid* convention used in [Euclid Collaboration: Romelli et al. 2025](#), where a tile denotes a unit sky region processed by the MER pipeline. Each tile is covered by a set of mosaics, one in each *Euclid* band.

² For more information on the VIS and MER data models, we refer the reader to the data product description page: <http://st-dm.pages.euclid-sgs.uk/data-product-doc/dmq1/>. It should be noted that the data model and the MER pipeline are constantly evolving. In this work, we use the data model 10 and the version 11.2 of the MER pipeline from February 2025, which is representative of the Q1 processing.

in I_E , which is typical of the EWS (see background estimations of [Euclid Collaboration: Scaramella et al. 2022](#); [Euclid Collaboration: Borlaff et al. 2022](#), who take into account the zodiacal light, Milky Way interstellar medium, and the cosmic infrared background).

2.1.2. Running the *Euclid* MER pipeline

The numerical tools required to run the SGS pipelines are grouped under the *Euclid* development environment. While EWS data are processed in dedicated data centres, for the specific needs of this study we use a Docker container equipped with this environment, in order to execute each step of the MER pipeline locally. We categorise those steps in several groups listed below, though we refer the reader to [Euclid Collaboration: Romelli et al. \(2025\)](#) for a more detailed description.

- Stacking and tiling with VIS background subtraction.
- Final mosaics production with MER additional local background subtraction.
- Detection, segmentation, and deblending of the objects.
- Input point-spread functions (PSFs) coaddition and selection of the reference PSF for each source based on its position.
- Photometry computation and morphology characterization for each source.
- Sérsic fitting on the source cutouts.
- Production of final MER catalogues combining the photometry, morphology, PSF and Sérsic fitting information for each source.

This work includes running the MER pipeline on the set of VIS calibrated single exposures defined in Sect. 2.1.1. The final MER VIS mosaic delivered by the pipeline and the final MER catalogue are extracted from the outputs. The VIS NoiseChisel background and the MER background are subtracted from this product.

2.2. Mock dwarf galaxies

To assess the capabilities of the MER pipeline for detecting dwarf galaxies, we inject such objects into single exposures, run the MER pipeline and verify if the injected objects appear in the final MER catalogue with the right parameters. This requires building a mock dwarf galaxy catalogue with realistic parameters and a dwarf injection routine.

2.2.1. Simulated dwarf galaxy parameters

The goal is to assemble a rather complete sample dwarf galaxies reported so far in the literature to estimate the capability of *Euclid* to recover them. We gathered catalogues of dwarf galaxies – including ultra-faint dwarfs and ultra-diffuse galaxies – at distance up to 120 Mpc, ensuring comprehensive coverage across the range of simulation distance (10 Mpc, 20 Mpc, 70 Mpc, and 100 Mpc), selected according to the distances explored in the ERO. The galaxies are located in all types of environments from the field to galaxy groups and clusters. We summarize the used catalogues together with their respective environment and distance in Table 1. Combining all the catalogues, we obtain a reference sample of 4861 galaxies. Based on available morphological information, the reference sample contains about 83% of dwarf ellipticals, and some irregulars show a mixed morphology with both star formation clumps and a diffuse component. Only models of galaxies corresponding to dwarf ellipticals are injected in

Table 1: Reference sample for simulated dwarf galaxies.

| Environment | Distance [Mpc] | References |
|-----------------|----------------|--|
| Local Group | < 3 | McConnachie (2012); Simon (2019) |
| Local Volume | < 12 | Carlsten et al. (2020) |
| Field and group | 10 – 120 | Merritt et al. (2016); Leisman et al. (2017); Román & Trujillo (2017); Greco et al. (2018); Forbes et al. (2020); Poulain et al. (2021); Marleau et al. (2021) |
| Virgo cluster | 16.5 | Ferrarese et al. (2020); Lim et al. (2020) |
| Fornax cluster | 20 | Eigenthaler et al. (2018); Venhola et al. (2017); Venhola et al. (2022) |
| Hydra I cluster | 51 | Iodice et al. (2020) |
| Perseus cluster | 72 | Marleau et al. (2025) |
| Coma cluster | 100 | Zaritsky et al. (2019) |

the simulations, as this morphological type has been dominating dwarf galaxy surveys, and such galaxies can serve as proxies for the diffuse component of late-type dwarfs. In Fig. 1, we show their size-luminosity relation.

The dwarf galaxies injected into the VIS images were modelled using a Sérsic profile (Sérsic 1963). For each galaxy, we set the Sérsic index to 0.8, i.e., the median value of the reference sample, as our study is focusing on the effect on the magnitude and effective radius (R_e) of the galaxies only. We randomly select the absolute magnitude and R_e in kpc by picking a galaxy from the reference sample. The drawn R_e and absolute magnitude M_g are then converted to arcsecond and apparent magnitude according to the simulation distance (D). The dwarfs are set to be round. At each D , we draw 100 galaxies considering only dwarfs at a similar distance or smaller to also test the detection of close-by faint ones, such as ultra-faint dwarfs in the Local Group.

To investigate the effect of the presence of a nucleus on the detection of the galaxy, we clone each simulated dwarf and model a nucleus at the centre by using a King profile (King 1966), leading to nearly 200 galaxies per simulation. Following the simulations of bright globular clusters from *Euclid* Collaboration: Voggel et al. (2025), we modelled a nucleus such that FWHM = 4 pc. The magnitude of the nucleus is determined from the linear relation $M_{g,nuc} = 0.5M_{g,gal} - 2.17$ between the galaxy and nucleus absolute magnitude shown in Fig. 2, fitted on the properties of nucleated dwarfs from Sánchez-Janssen et al. (2019) in the Virgo galaxy cluster, Eigenthaler et al. (2018) and Ordenes-Briceño et al. (2018) in the Fornax cluster, and Poulain et al. (2021) in field and galaxy groups environment.

The position of each dwarf on the exposures is defined in order to simulate about 200 objects at each distance. This number is chosen to obtain reliable statistics without overcrowding the exposures. To avoid galaxy overlap, we define a square area of side from $9R_e$ to $42R_e$ around each dwarf where no other dwarf is injected. The smallest area ensures having enough sky to model the galaxy (as explained in Sect. 2.4), whereas areas larger than $9R_e$ are defined as a function of D so that ~200 objects are distributed all over the exposure.

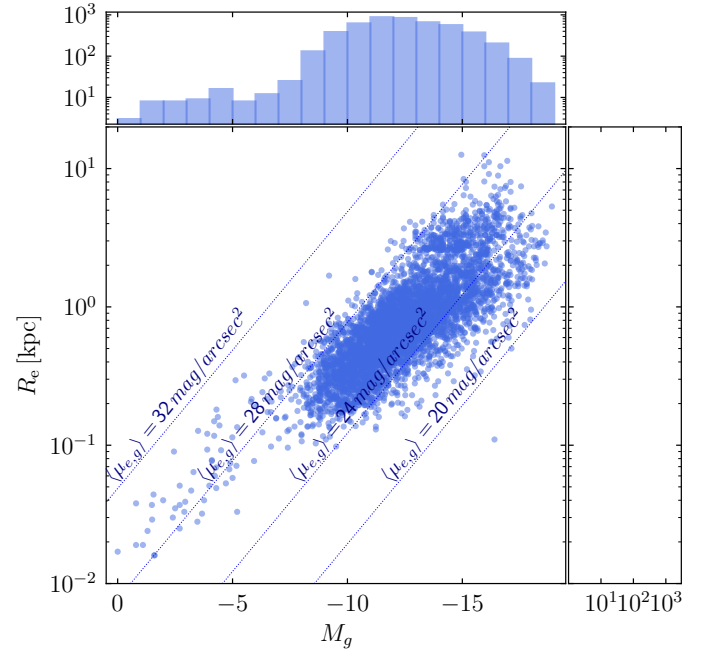


Fig. 1: Scaling relation between the effective radius and absolute magnitude in the g -band of the dwarfs galaxies in the reference sample. We indicate the average surface brightness within R_e in the g -band with dotted lines.

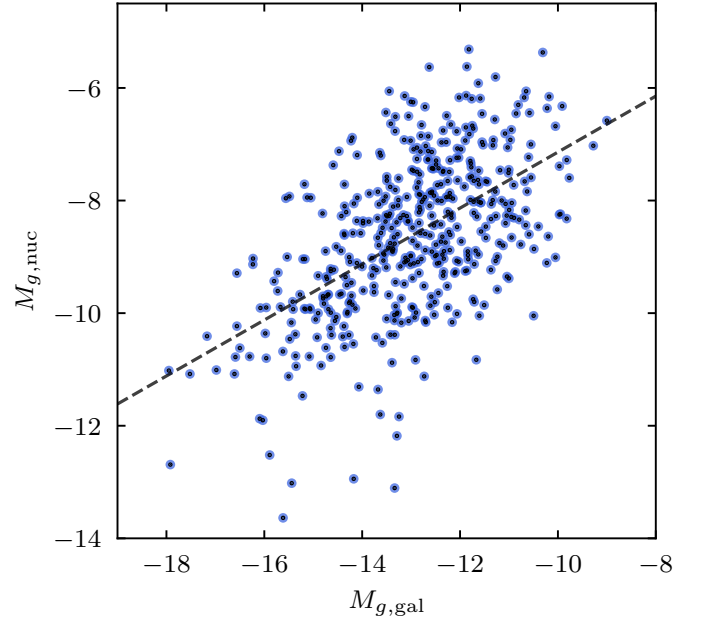


Fig. 2: Relation between the absolute magnitude in the g -band of the nucleus and dwarf galaxy host from for nucleated dwarf galaxies in the Virgo and Fornax clusters as well as in the field and galaxy groups. The linear fit is shown with a dashed line.

2.2.2. Injecting mock dwarf galaxies in *Euclid* calibrated single exposures

We develop the Python code LSBSim to inject dwarfs and their nuclei in real EWS images. For a given *Euclid* VIS calibrated single exposure, LSBSim receives a list of galactic parameters (right ascension, declination, total magnitude, position angle, effective radius, ellipticity, and Sérsic index). It has also as input

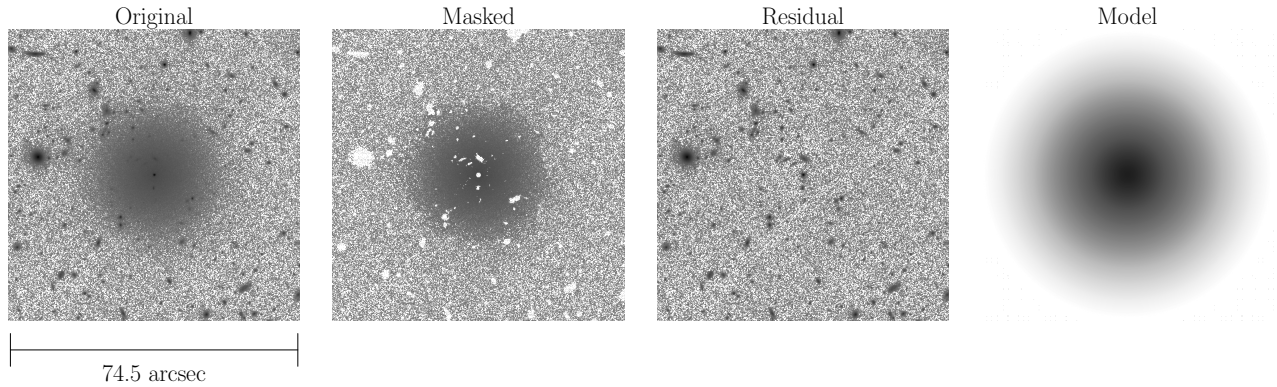


Fig. 3: Summary of the Galfit fitting strategy, including, from left to right: the original image (i.e. the cutout of an injected dwarf galaxy at 10 Mpc), the masked image obtained with a combination of MTObjects and Source Extractor segmentation maps, the residual image obtained by subtraction of the original image with the model, and the model image.

a list of nuclear star cluster parameters (right ascension, declination, total magnitude, ellipticity, core radius, and tidal radius). Then, LSBSim scans the 144 quadrants to inject these nearby objects. The program uses stamps where galaxies are generated by the GalSim Python package (Rowe et al. 2014) and then injected at the specified world coordinate system (WCS) location on the different quadrants. We convolve the injected objects with the *Euclid* VIS PSF (calculated from ERO data in Urbano et al. 2025; Saifollahi et al. 2025a, see also Cuillandre et al. 2025a) and add Poisson noise to these stamps before the injection. The native GalSim package contains a Sérsic function used for generating dwarf galaxies. For the nuclei, we develop a function to allow GalSim to handle the King model.

This procedure allows us to update the single exposure data cubes with the injected objects, more specifically the science image and the Poisson-noise root mean square map, quadrant by quadrant, with the injected Local Universe objects. We need to update the background files corresponding to those single exposures as well. To do this, we run NoiseChisel on each quadrant containing the injected Local Universe objects, using exactly the same configuration parameters as in the VIS pipeline. This results in a complete set of MER pipeline input for each exposure.

After the MER pipeline run, we extract the MER mosaics before and after background subtraction, and the final MER catalogues. Those products are analysed in the following sections.

2.3. Sérsic model fitting with Galfit

In the MER catalogue, the Sérsic parameters of galaxies are estimated through fitting each source cutout with SourceExtractor++ runs included in the pipeline. We compare the obtained parameters with the injected ones, and with those measured by ourselves using the method detailed in the next paragraphs.

We produce a cutout in the final MER mosaic for each of the injected dwarfs with a side length of nine effective radii, as suggested in Poulain et al. (2021) to encompass enough background around the dwarf galaxy. We use the Galfit (Peng et al. 2002) software to fit the dwarfs on each of our cutouts. In particular, we use initial parameters close to the input ones and we also fit a tilted plane background with 0 as initial level entered in the software. This approach requires masking all sources, except for the object to be fitted. However, the number of injected dwarf galaxies does not allow manual masking for each of the associated cutouts. As in Marleau et al. (2025), we use a combination

of segmentation maps produced by MTObjects (Teeninga et al. 2015) and Source Extractor (Bertin & Arnouts 1996), from which we remove the central detection to prevent the galaxy of interest from being masked. We mask a small circular region at the centre of each galaxy, taking into account the presence of a nucleus and its size. This combination brings out the best in both software packages, respectively providing generous mask sizes for extended objects and sensitivity to compact sources. This strategy is exemplified in Fig. 3.

2.4. Visual inspection

One expert inspects each cutout, classifying the dwarfs into two categories: “Detected by eye” when the object is visually identified as a dwarf and “Undetected” when the object’s nature is uncertain or there is no visual detection. The human eye still outperforms segmentation algorithms in detecting and identifying dwarf galaxies, even with a small number of classifiers and when these algorithms are optimised for LSB (see, for instance, a performance comparison between visual inspection and MTObjects in Müller & Jerjen 2020).

3. Results

3.1. Dwarf galaxy detection

In this subsection, we assess the capabilities and limitations of MER for detecting Local Universe dwarf galaxies.

We crossmatch the injected dwarf coordinates with the final MER catalogues (using a search radius R_{SEARCH} which is typically R_e and is further discussed in Appendix B). We find, in particular, a completeness of 91 % for $SB_e \in [21, 24]$, and 54 % for $SB_e \in [24, 28]$ in mag arcsec^{-2} (see Appendix D for full results). These values represent upper limits which do not take into account any contaminant correction, including confusion with background galaxies.

The final, corrected results are shown in Fig. 4 and detailed below. These histograms illustrate the detected fraction of dwarf galaxies, depending on SB_e and R_e . These fractions in each bin are reported in Tables 2 and 3, respectively. We complete the analysis by separating the dwarfs based on their distance, and reproducing the same plots in Appendix E.

We detail below the different detection scenarios.

- Simple detection in the MER catalogue: the injected dwarf has one match in the final MER catalogue within R_{SEARCH} .

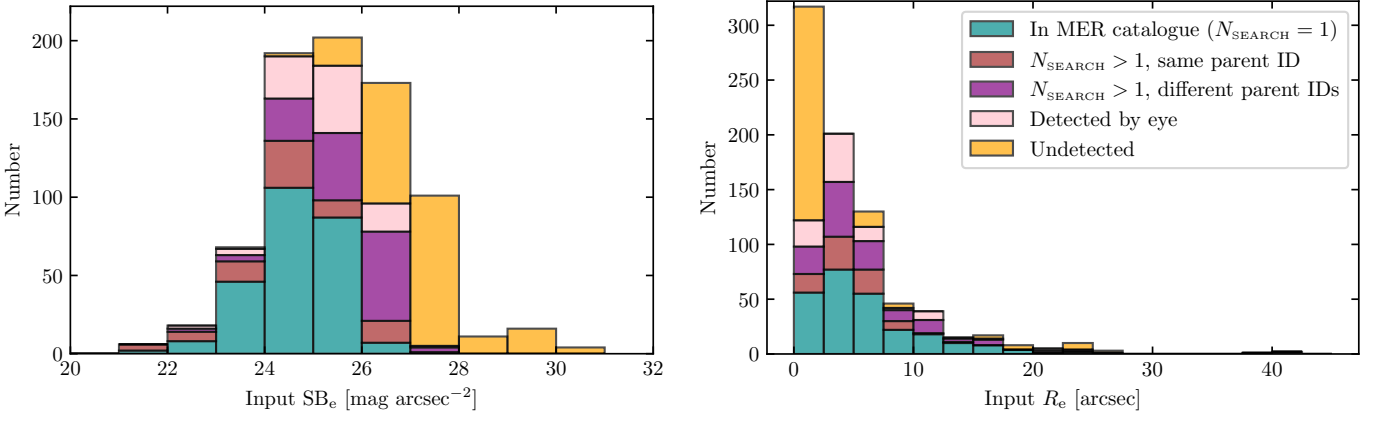


Fig. 4: Histograms of the input SB_e (left panel) and the input R_e (right panel), colour-coded according to their detection by eye and in the MER catalogue, N_{SEARCH} being the number of MER sources found by using the search radius R_{SEARCH} for the crossmatch. It is worth noting that the dwarfs in MER catalogues and those with $N_{\text{SEARCH}} > 1$ are also detected by eye. In Appendix C, we also provide the histogram of $\langle \mu_1 \rangle$ as defined in Euclid Collaboration: Marleau et al. (2025). In this plot, all the dwarfs (nucleated or not) are included.

Table 2: Comparison between the detection statistics across different SB_e bins. Column (1) gives the SB_e bin. Columns (2) indicates the number of injected dwarfs. The remaining columns are the number of dwarfs that are (3) present in the final MER catalogue as one single object, (4) present in the final MER catalogue as one or several objects sharing the same parent ID, (5) present in the final MER catalogue as one or several objects sharing or not the same parent ID(s), and (6) visually detected, whether or not they are present in the final MER catalogue. As a result, columns (3) to (5) are cumulative. Columns (2) to (6) are given in number and in percent of the injected dwarfs in the corresponding surface brightness bin. In this table, all the dwarfs (nucleated or not) are included.

| SB_e [mag arcsec $^{-2}$] | Input dwarfs | In MER catalogue | Single parent ID | Single or multiple parent ID(s) | Detected by eye |
|------------------------------|--------------|------------------|------------------|---------------------------------|-----------------|
| (1) | (2) | (3) | (4) | (5) | (6) |
| 21–22 | 6 (100 %) | 2 (33 %) | 6 (100 %) | 6 (100 %) | 6 (100 %) |
| 22–23 | 18 (100 %) | 8 (44 %) | 14 (78 %) | 16 (89 %) | 18 (100 %) |
| 23–24 | 68 (100 %) | 46 (68 %) | 59 (87 %) | 63 (93 %) | 67 (99 %) |
| 24–25 | 193 (100 %) | 106 (55 %) | 136 (70 %) | 163 (84 %) | 190 (98 %) |
| 25–26 | 202 (100 %) | 87 (43 %) | 98 (49 %) | 141 (70 %) | 184 (91 %) |
| 26–27 | 173 (100 %) | 7 (4 %) | 21 (12 %) | 78 (45 %) | 96 (55 %) |
| 27–28 | 101 (100 %) | 0 (0 %) | 1 (1 %) | 4 (4 %) | 5 (5 %) |
| 28–29 | 11 (100 %) | 0 (0 %) | 0 (0 %) | 0 (0 %) | 0 (0 %) |
| 29–30 | 16 (100 %) | 0 (0 %) | 0 (0 %) | 0 (0 %) | 0 (0 %) |
| 30–31 | 4 (100 %) | 0 (0 %) | 0 (0 %) | 0 (0 %) | 0 (0 %) |

To visualize the characteristics of such objects, we plot the parameter space (i.e. the input R_e as a function of the input total magnitude I_e) in Fig. 5. We observe that, for a given magnitude, the final MER catalogue misses the most extended galaxies. The region of the parameter space beyond 22.5 as total input magnitude in I_e is dominated by objects that are not detected. Combining all SB_e bins up to 28 mag arcsec $^{-2}$, 34 % of the injected dwarf galaxies are recovered as single sources in the final MER catalogue. For $SB_e < 24$ mag arcsec $^{-2}$ (regular dwarf regime), 61 % of the injected dwarfs are recovered in the final MER catalogue. For $SB_e > 24$ mag arcsec $^{-2}$ (LSB regime), 30 % of the injected dwarfs are recovered in the final MER catalogue.

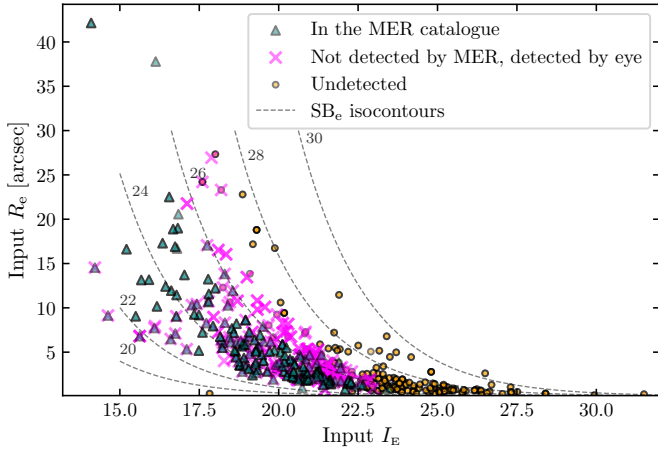
- Multiple detection in the MER catalogue: the injected dwarf is associated with multiple MER sources with different IDs within R_{SEARCH} . In such cases, the dwarf appears fragmented into several areas in the segmentation map generated during

the MER pipeline run (see an example in Fig. 6). This effect arises from its deblending step. The MER pipeline assigns the same value in the PARENT_ID column of the final MER catalogue (hereafter referred to as the “parent ID”) to all sources that were initially segmented together but later separated during deblending. We can then distinguish between two subtypes of detection:

- Single parent ID detection: the dwarf galaxy was correctly segmented but split into multiple sources during deblending. In this case, all regions making up the dwarf galaxy share the same parent ID, and it is possible to regroup them afterwards to measure the properties of the object. Combining all SB_e bins up to 28 mag arcsec $^{-2}$, 44 % of the injected dwarf galaxies are recovered as single sources or multiple sources with the same parent ID in the final MER catalogue. For $SB_e < 24$ mag arcsec $^{-2}$ (regular dwarf regime), 86 % of the in-

Table 3: Similar to Table 2, but now binning the data in R_e instead of in SB_e .

| R_e [arcsec] | Input dwarfs | In MER catalogue | Single parent ID | Single or multiple parent ID(s) | Detected by eye |
|----------------|--------------|------------------|------------------|---------------------------------|-----------------|
| (1) | (2) | (3) | (4) | (5) | (6) |
| 0–2.5 | 317 (100 %) | 56 (18 %) | 73 (23 %) | 98 (31 %) | 122 (38 %) |
| 2.5–5 | 201 (100 %) | 77 (38 %) | 107 (53 %) | 157 (78 %) | 201 (100 %) |
| 5–7.5 | 130 (100 %) | 55 (42 %) | 77 (59 %) | 103 (79 %) | 116 (89 %) |
| 7.5–10 | 46 (100 %) | 22 (48 %) | 30 (65 %) | 40 (87 %) | 42 (91 %) |
| 10–12.5 | 39 (100 %) | 18 (46 %) | 19 (49 %) | 31 (79 %) | 39 (100 %) |
| 12.5–15 | 15 (100 %) | 10 (67 %) | 11 (74 %) | 14 (93 %) | 15 (100 %) |
| 15–17.5 | 17 (100 %) | 8 (47 %) | 8 (47 %) | 13 (76 %) | 14 (82 %) |
| 17.5–20 | 8 (100 %) | 4 (50 %) | 4 (50 %) | 4 (50 %) | 4 (50 %) |
| 20–22.5 | 5 (100 %) | 1 (20 %) | 1 (20 %) | 3 (60 %) | 5 (100 %) |
| 22.5–25 | 10 (100 %) | 2 (20 %) | 2 (20 %) | 4 (40 %) | 4 (40 %) |
| 25–27.5 | 3 (100 %) | 0 (0 %) | 0 (0 %) | 1 (33 %) | 1 (33 %) |
| 37.5–40 | 1 (100 %) | 1 (100 %) | 1 (100 %) | 1 (100 %) | 1 (100 %) |
| 40–42.5 | 2 (100 %) | 2 (100 %) | 2 (100 %) | 2 (100 %) | 2 (100 %) |

**Fig. 5:** Input R_e as a function of the total magnitude in I_E used to inject the dwarfs. They are colour-coded according to their detection (in the final MER catalogue, only by eye, or not detected).

jected dwarfs are recovered in the final MER catalogue. For $SB_e > 24 \text{ mag arcsec}^{-2}$ (LSB regime), 38 % of the injected dwarfs are recovered in the final MER catalogue.

- Multiple parent IDs: the faint dwarf is segmented into multiple regions assigned to different parent IDs even before deblending. Such objects are difficult to recover afterwards.
- Contamination by other sources: the dwarf has MER detections within R_{SEARCH} , but these correspond to background sources and/or the dwarf cannot be identified as such. Visual inspection, along with a crossmatch between the input dwarf catalogues and the MER mosaic generated from a pipeline run without any injected dwarfs, ensures that such cases are not counted among the detected dwarfs.
- No detection in the MER catalogue. This occurs either when the dwarf is too faint to be detected and there are no background sources within R_{SEARCH} , or when its mask is mistakenly

merged with that of a nearby bright extended object (including, but not limited to, Milky Way stars, as exemplified in Fig. 7).

The detection limit of the catalogue (cyan + brown bars in Fig. 4), as well as that of the visual detection (purple + rose bars in Fig. 4) is between $SB_e = 27 \text{ mag arcsec}^{-2}$ and $SB_e = 28 \text{ mag arcsec}^{-2}$ (corresponding to a signal-to-noise ratio between 2 and 3). Together with Fig. 5, we can also highlight $I_E = 22.5$ as the threshold distinguishing a regime dominated by detected dwarf galaxies from another regime dominated by dwarf galaxies which are not. Below $R_e \approx 3''$, very few detections are made.

We now explore whether the initial VIS background subtraction using NoiseChisel or the subsequent MER local background subtraction have an impact on the detection of dwarf galaxies. To do so, we compare the final MER mosaic, the mosaic prior to the MER background subtraction but after the VIS background subtraction (“VIS BGSUB mosaic” hereafter), and the mosaic before both background subtractions as a reference point (“NOBG mosaic” hereafter). We extract the VIS BGSUB mosaic as an intermediate product produced during the MER pipeline run. The NOBG mosaic is not a standard product delivered during the MER pipeline run. However, it can be easily generated with a second run of the pipeline using constant background files instead of the VIS background files, and by extracting the mosaic before the second (local MER) background subtraction. The visual inspection for the final mosaic is repeated for the “VIS BGSUB mosaic” and the “NOBG mosaic” (see Appendix F), and this analysis shows the background has no significant impact on the dwarf detection.

Finally, we also investigate the impact of the presence or absence of a nucleus on detection, by reproducing in Fig. 8 and Fig. 9 the histogram of the input SB_e from Fig. 4, this time separating nucleated dwarfs from non-nucleated ones. Detection slightly favours nucleated dwarfs. When summing all surface brightness bins up to $28 \text{ mag arcsec}^{-2}$, 42 % of the injected non-nucleated dwarfs are recovered, compared to 46 % for nucle-

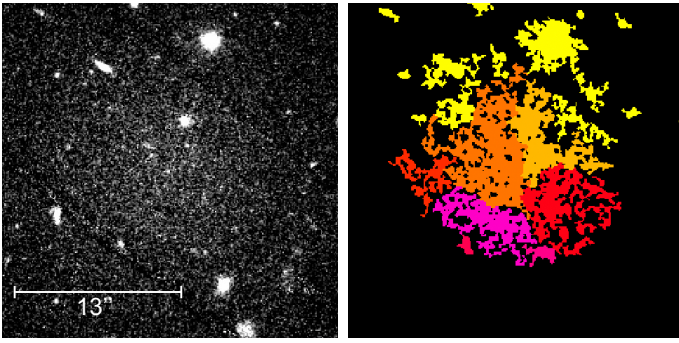


Fig. 6: Example of segmentation and deblending for an injected dwarf galaxy (left panel). The associated mask (right panel) is divided into multiple sources, differentiated by different colours.

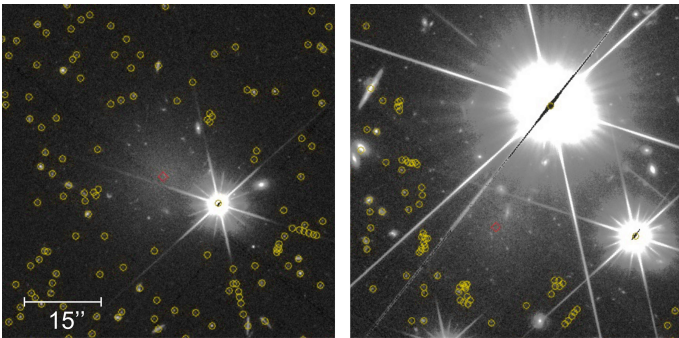


Fig. 7: Examples of non-detection of a dwarf galaxy by the MER pipeline in the vicinity of a Milky Way star. The MER pipeline detections are labelled with blue circles, the injected dwarfs are labelled with red squares.

ated dwarfs. Specifically, in the non-LSB regime, 83 % of non-nucleated dwarfs are detected versus 89 % of nucleated ones. In the LSB regime, 37 % of non-nucleated dwarfs are detected compared to 40 % for nucleated dwarfs. The largest difference is found in the 25–26 mag arcsec⁻² bin, amounting to 9 %.

3.2. Dwarf galaxy parameter measurements

The MER pipeline was developed with a strong focus on high-quality photometry for compact sources, such as distant galaxies, in order to meet the requirements of cosmology, the core science of the *Euclid* mission. In this subsection, we examine the parameters returned by the final MER catalogue for diffuse sources in the Local Universe and assess the ability of the pipeline to support science for which it was not originally optimised. Then, we explore the impact of the different background subtractions.

3.2.1. Parameters in output of the MER pipeline

Based on the crossmatch between the input catalogue of injected galaxies and the list of dwarfs detected as a single source in the final MER catalogue, we can compute the difference between the measured magnitude (derived from the MER catalogue column FLUX_VIS_SERSIC) and the input magnitude as a function of R_e (Fig. 10). We observe two main effects: a scatter and a flux loss which increases with the radius.

Regarding the scatter in the recovered magnitude, we interpret cases where the flux is overestimated as instances where bright objects (including, but not exclusively, overlapping stars)

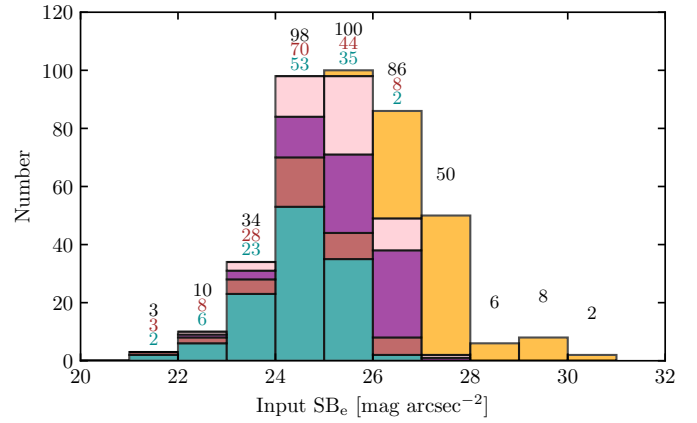


Fig. 8: Identical to the left panel of Fig. 4, but only for the non-nucleated dwarfs. Above each bin, the number of injected dwarfs is shown in black, the number of dwarfs recovered as either a single MER source or as multiple fragments with the same parent ID is shown in brown, and the number recovered as a single MER source is shown in cyan.

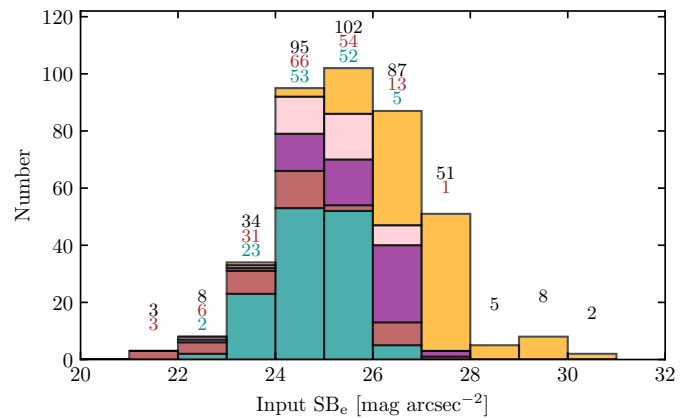


Fig. 9: Identical to Fig. 8, but for nucleated dwarfs.

remain within the detected galaxy. To explain the more common cases of flux underestimation, we note that the MER segmentation masks may not be extended enough to encompass most of the flux of the dwarf galaxy. This can lead to the production of cutouts that are too small for a proper fitting by *SourceExtractor++*.

Regarding the flux loss increasing with the radius, this happens beyond an effective radius of 10'' (it reaches $\Delta I_e \approx 1.5$ at $R_e \approx 40''$). Such an effect may indicate a local background oversubtraction. This becomes problematic when the object for which we aim to measure photometry exceeds the size of a cell used to estimate the background. The impact of the different background subtractions applied during the MER pipeline run is explored in the following subsections. We repeat the model fitting with *GalFit* described in Sect. 2.3 for the final MER mosaic is repeated for the “VIS BGSUB mosaic” and the “NOBG mosaic”.

3.2.2. Impact of the MER background

To further test the impact of the MER background subtraction, we can compare the final, fully background-subtracted mosaic with the intermediate product where only the NoiseChisel VIS background has been applied (no local MER background subtraction).

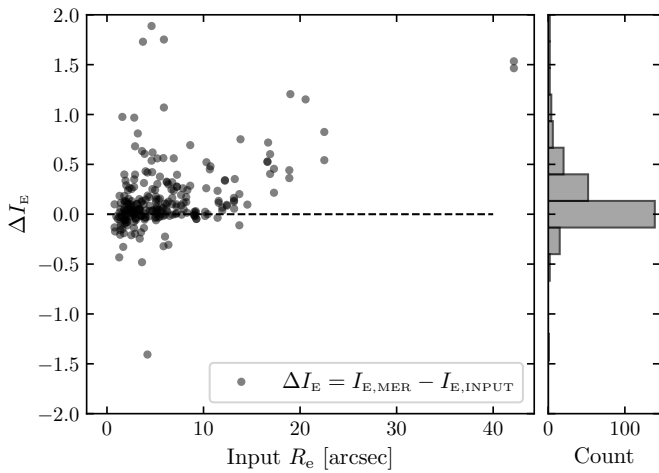


Fig. 10: Difference between the SourceExtractor++ measured magnitude in the final MER catalogue and the input magnitude of injected dwarfs as a function of R_e , for all dwarfs detected in the final MER catalogue.

Figure 11 displays the impact of each background subtraction on the Galfit total I_E magnitude ($\Delta I_E = I_{E,BGSUB} - I_{E,NOBG}$) as a function of the input R_e . The large scatter at very small R_e corresponds to the regime in which dwarf galaxy identification and model fitting become challenging, and where the PSF may significantly affect the derived parameters. The right panel shows the impact of the MER local background subtraction. As also observed in Fig. 10, a difference in the magnitudes is visible beyond $R_e = 10''$, with the deviation increasing until reaching 1.5 magnitude at $R_e \approx 40''$. Thus, after the MER local background subtraction, the structural parameters of the dwarfs with $R_e \geq 10''$ are modified. An example of a dwarf galaxy whose structural parameters are significantly affected after the second background subtraction is presented in Fig. 12.

3.2.3. Impact of the VIS background

We test the effect of the initial NoiseChisel VIS background subtracted mosaic by comparing it to the custom mosaic where no background subtraction is applied.

In order to check whether the initial NoiseChisel background subtraction impacts the measured parameters of the dwarf galaxies, we perform the same test as before by comparing the magnitudes measured on the images without any background subtraction and after this first background subtraction (respectively the “NOBG mosaic” and the “VIS BGSUB mosaic”). This is what is shown on the left panel of Fig. 11. We observe that the trend observed for galaxies detected by eye corresponds to a null magnitude difference. Thus, this first background subtraction does not impact the structural parameters of the detected dwarfs.

4. Discussion

4.1. Making the most of MER pipeline products

Provided we are able to merge the dwarf galaxy fragments that share the same parent ID (a step that must be carried out after the MER pipeline run, since the pipeline itself neither performs this operation nor outputs the parameters of the re-merged sources), the final MER catalogue is nearly 90 % complete down to a surface brightness of $24 \text{ mag arcsec}^{-2}$. The final MER catalogue pa-

rameters remain reliable for galaxies with a size up to $R_e = 10''$, beyond which a flux loss is observed. The analysis and comparison of the final MER mosaic, the VIS BGSUB mosaic, and the NOBG mosaic allow us to observe that this flux loss emerges with the subtraction of the second, MER local background. Indeed, we do not observe any changes in the dwarf galaxy parameters when subtracting only the VIS background, but we observe the flux loss when subtracting the MER background from the VIS background subtracted image.

The final MER catalogue is derived from the final MER mosaic which is MER background subtracted (i.e. the parameters of the dwarf galaxies before the local background subtraction are not measured, and thus are not available in the MER catalogues). The safest way to recover the parameters of Local Universe dwarf galaxies (particularly beyond $R_e = 10''$) is then to run outside of the MER pipeline a model fitting program on the final mosaic or its cutouts, after having first re-added the second MER local background (thereby reverting to the VIS BGSUB mosaic, subtracted only from the VIS background). This can be easily achieved using the background maps (“BGMOD”) provided in the ESA Science Archive.

It is important to highlight that the VIS background is estimated at the quadrant scale (approximately $3' \times 3'$), which could lead to flux loss for objects approaching or exceeding this size. However, most dwarf galaxies in the Local Universe do not reach this size. This suggests that the VIS background subtracted products from the *Euclid* SGS pipelines are fully compliant with the science of most dwarfs. This result cannot be extended to studies concerning the extended halos of giant galaxies, including their tidal features, and intracluster light. Indeed, they are typically more extended, and thus, are more likely to be affected by this quadrant scale limitation.

A detection approach relying solely on the MER catalogues would miss the most extended and faint dwarf galaxies (notably more than 50 % of those between 24 and $28 \text{ mag arcsec}^{-2}$ in effective surface brightness, beyond which dwarfs are no longer identifiable in *Euclid* images) as well as those located near bright and/or extended objects, which tend to be jointly segmented.

To overcome some of the limitations mentioned above, one may propose possible modifications to the SGS pipelines. One possible solution to make the SGS pipelines LSB-compliant at the scale of a full *Euclid* field of view (FoV) would be to replace the current quadrant-by-quadrant VIS background estimation with a FoV-scale approach (that is, first aligning the background levels of each quadrant, then applying NoiseChisel to a full VIS exposure composed of all quadrants, rather than processing each quadrant independently). To avoid flux loss in the output MER catalogues, an additional object parameter measurement step would need to be introduced in the MER pipeline before the local background subtraction (preferably using an LSB-optimised segmentation and deblending tools such as MObjects). In the course of this catalogue production procedure, it would be desirable to reduce the area around bright stars where sources cannot be detected. This can be achieved using the same LSB-optimised segmentation and deblending algorithms mentioned earlier.

4.2. Limitations of this study

Several studies are expected to build upon this work. Two promising directions are the inclusion of colour information and the exploration of a wider range of injected dwarf galaxy morphologies. This subsection outlines these two avenues.

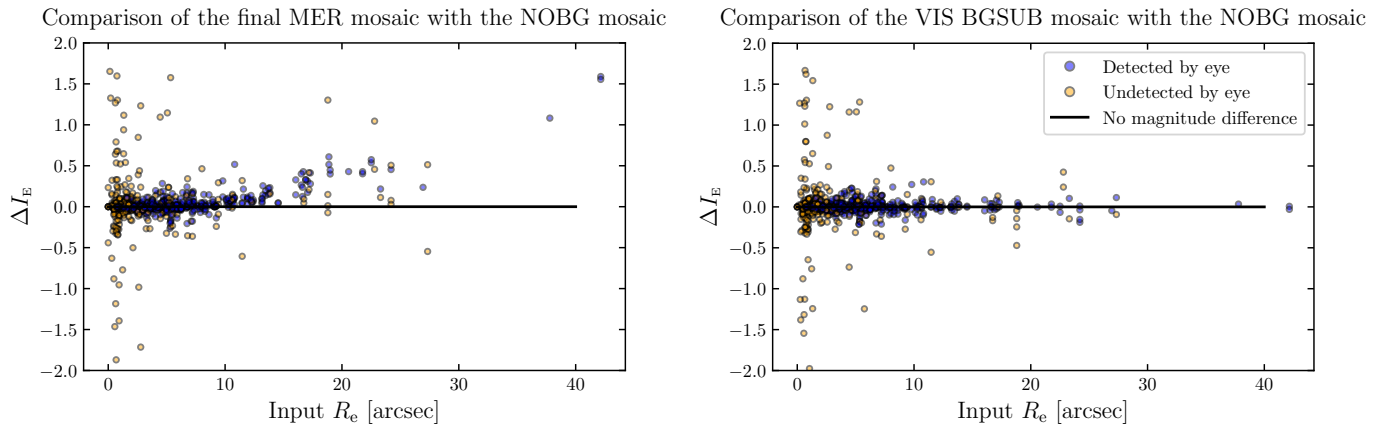


Fig. 11: The magnitude difference $\Delta I_E = I_{E,\text{BGSUB}} - I_{E,\text{NOBG}}$ as a function of the input effective radius, for the final MER mosaic and the VIS BGSUB mosaic cases. The total magnitudes are obtained using *Galfit*.



Fig. 12: Example of a dwarf galaxy successfully detected in the VIS BGSUB mosaic (left panel). The second background subtraction affects its appearance, and consequently its structural parameters, in the final MER mosaic (right panel). The same scale is used for both images. It is worth noting that this is the brightest ($I_E = 18$) and most extended galaxy in our sample at 10 Mpc, and that such objects are statistically rare in the Local Universe.

For this paper, we have considered only the I_E band, as its greater depth and higher resolution compared to the NIR bands make it the optimal detection band in *Euclid*. This is especially true in the Local Universe, where dwarf galaxies that are undetected in the I_E band are not expected to be detectable in any of the NIR bands. Nevertheless, a new study will be required to test the impact of background subtraction on the colours of dwarf galaxies. Indeed, not only can the second background subtraction performed by MER alter the measured colour of Local Universe objects, but a first source of error may arise from the initial background subtraction, which is calculated differently in the VIS and NIR pipelines (especially, in the NIR pipeline, the background is computed at the scale of each of its 16 single $10' \times 10'$ detectors, see also *Euclid Collaboration: Polenta et al. (2025)*). Including the study of the NIR bands would also allow us to assess how colour selection can improve the detection and identification of dwarf galaxies (in particular distant ones, which cannot be distinguished from background sources using the I_E image alone).

Also, in this paper, we have only injected elliptical galaxies, as they represent the most common type among the real dwarf catalogues used to find the mock dwarf parameters. We also limited ourselves to selecting galaxies already identified as dwarfs in those catalogues, which, by definition, led us to omit

dwarfs with rarer morphologies that may not have been classified as such. Indeed, our goal here was to cover a realistic parameter space for dwarf galaxies. However, to diversify the nature of the injected dwarfs, it will then be necessary to use more realistic dwarf galaxy models (including for dwarf irregulars), likely derived from simulations (e.g., mock images extracted from *IllustrisTNG*, presented in *Nelson et al. 2018*), to better determine the multi-band detection capabilities and limits for dwarfs with different morphological types and star-formation histories. The inclusion of dwarf galaxies with star-formation clumps will also help assess the fragmentation of such objects into multiple sources (linked or not by the same parent ID) by MER.

Finally, it is worth noting that the results presented in this paper are more applicable to dwarf galaxies in the field, in the sense that each mock galaxy is sufficiently isolated from its neighbours so that its light does not affect their detection or parameter fitting (as is often the case in the field). The effect of dwarf galaxy clustering will be addressed in a future paper focusing on the injection of mock dwarf galaxies in different environments (including galaxy clusters).

4.3. Comparison to other *Euclid* works

Several other *Euclid* papers also discuss the detection of dwarf galaxies, such as *Euclid Collaboration: Marleau et al. (2025)* and *Cuillandre et al. (2025b)*, respectively in the context of Q1 and ERO Perseus data. One of the detection limits highlighted in these two studies, as well as in ours, is the total magnitude detection threshold.

In our paper, we have highlighted $I_E = 22.5$ as the threshold distinguishing a regime dominated by detected dwarf galaxies from another regime dominated by dwarf galaxies which are not. *Euclid Collaboration: Marleau et al. (2025)* report detections up to about 1 magnitude fainter, based on measurements from the MER catalogue. This can be explained, on the one hand, by the use of colour images from *Euclid*, which may facilitate the identification of small and/or faint dwarfs and their distinction from background sources. On the other hand, it may be due to less reliable photometry in the MER catalogue for these faint objects (as seen in Fig. 10, a 1 magnitude difference between the real and measured total magnitude is possible).

Finally, the objective of our paper is to assess the capability of *Euclid* standard pipeline products to probe Local Universe

dwarf galaxies. A different study, which is beyond the scope of this paper, will consist in the injection of a large number of dwarfs at various distances. It would be necessary to establish predictions on the detection of the faint end of the dwarf galaxy luminosity function as a function of redshift and environment. Such a work has already been initiated for *Euclid* images in the specific case of estimating the galaxy luminosity function in the ERO Perseus data. This study, described in Appendix B of Cuilandre et al. (2025b), reveals as well a break and a drop in completeness at $I_e = 22.5$ (see Fig. B.6 of this paper).

4.4. Prospects and generalisation to other wide surveys

Using the MER catalogues could be an efficient way to build a training set for machine learning and deep learning algorithms, in order to automatically identify numerous dwarf galaxies in *Euclid* images. However, it should be noted that in a training sample solely based on MER catalogue detections, LSB dwarfs will be underrepresented.

Investigating the effects of background subtraction from the *Euclid* pipeline serves as a valuable test-bed for other wide surveys, as it employs two widely used subtraction methods: one designed to be LSB-compliant (NoiseChisel) and another optimised for compact source analysis (local background subtraction, here applied through SourceXtractor++). Several current and future wide surveys use a local background subtraction, such as the DESI Legacy imaging surveys (e.g., the Dark Energy Camera Legacy Survey DECaLS, Dey et al. 2019), while others are still developing this step of their image processing pipeline, as is the case for the Vera Rubin Observatory's Legacy Survey of Space and Time (Ivezić et al. 2019; Brough et al. 2020; Watkins et al. 2024). Such consideration of the treatment of the background is also relevant for missions on longer timescales (e.g., *Nancy-Roman-Grace*: Koekemoer & Roman Deep Fields Working Group 2023 and ARRAKIS: Guzmán 2024). Our study demonstrates that only the first method reliably preserves Local Universe dwarf parameters.

5. Conclusions

Achieving high completeness in the detection of dwarf galaxies down to the LSB regime is crucial for studies of galaxy evolution and near-field cosmology. The wide survey of the *Euclid* Space Telescope will unveil the LSB Universe with high resolution and deep VIS and NIR imaging over a large portion of the extragalactic sky, as demonstrated by early works on its first images. In this study, we measure the dwarf detection ability of *Euclid* by the injection of mock dwarfs and nuclei into individual exposures. We run the EWS MER pipeline and analyse its products in the VIS band. The MER pipeline includes background subtractions at different scales: one at the scale of a VIS quadrant, and the other at a local scale. We investigate the impact of these subtractions on the detection and parameter measurement of dwarf galaxies.

- Although the MER pipeline is fine-tuned for cosmology rather than LSB science, its final catalogues exhibit a high level of completeness for dwarf galaxies having $SB_e \leq 24 \text{ mag arcsec}^{-2}$ (86 %). Beyond this surface brightness, the MER catalogues still successfully recover a fraction of the injected dwarf galaxies (38 %).
- The background subtractions performed by the MER pipeline do not affect the detections.

- The local background subtraction causes a flux loss in dwarf galaxies larger than $R_e = 10''$. Re-adding this background (easily achievable using the final mosaics and the background maps provided by MER) followed by parameter measurements on these mosaics is sufficient to correct this issue. The extracted dwarf parameters remain accurate until the galaxy reaches arcminute scales, with the upper limit corresponding to that of a VIS quadrant (i.e., $3'$). Typically, Local Universe dwarf galaxies do not reach this size.

Including the NIR bands will make it possible to assess the impact of colour on the identification of dwarf galaxies. A future study will include this analysis, as well as the injection of more complex and realistic dwarf galaxies.

Identifying all LSB dwarfs that are intrinsically detectable by *Euclid*, as well as studying Local Universe objects more extended than $3'$ (typically giant galaxies, their tidal features, and ICL) require replacing the background subtractions applied in the MER pipeline by an alternative post-processing of the calibrated VIS single exposures, which are fully LSB-compliant.

The results described in this article help understanding background subtraction effects of both LSB compliant methods and local background subtraction methods, thus providing useful insight for current and upcoming deep surveys.

Acknowledgements. The authors thank Thomas Oliveira, Nicolas Mai and Samuel Rusterucci for insightful discussions. Junais is funded by the European Union (MSCA EDUCADO, GA 101119830 and WIDERA ExGal-Twin, GA 101158446). The Euclid Consortium acknowledges the European Space Agency and a number of agencies and institutes that have supported the development of Euclid, in particular the Agenzia Spaziale Italiana, the Austrian Forschungsförderungsgesellschaft funded through BMK, the Belgian Science Policy, the Canadian Euclid Consortium, the Deutsches Zentrum für Luft- und Raumfahrt, the DTU Space and the Niels Bohr Institute in Denmark, the French Centre National d'Etudes Spatiales, the Fundação para a Ciência e a Tecnologia, the Hungarian Academy of Sciences, the Ministerio de Ciencia, Innovación y Universidades, the National Aeronautics and Space Administration, the National Astronomical Observatory of Japan, the Nederlandse Onderzoekschool Voor Astronomie, the Norwegian Space Agency, the Research Council of Finland, the Romanian Space Agency, the State Secretariat for Education, Research, and Innovation (SERI) at the Swiss Space Office (SSO), and the United Kingdom Space Agency. A complete and detailed list is available on the Euclid web site (<http://www.euclid-ec.org>). M.P. and A.V. are supported by the Academy of Finland grant No. 347089.

References

- Abazajian, K., Adelman-McCarthy, J. K., Agüeros, M. A., et al. 2003, *AJ*, 126, 2081
- Abazajian, K., Zheng, Z., Zehavi, I., et al. 2005, *ApJ*, 625, 613
- Abraham, R. G. & van Dokkum, P. G. 2014, *PASP*, 126, 55
- Aihara, H., Arimoto, N., Armstrong, R., et al. 2017, *Publications of the Astronomical Society of Japan*, 70, S4
- Akhlaghi, M. 2019, *IAU Symposium* 335, arXiv:1909.11230
- Akhlaghi, M. & Ichikawa, T. 2015, *ApJS*, 220, 1
- Bertin, E. & Arnouts, S. 1996, *A&AS*, 117, 393
- Bertin, E., Mellier, Y., Radovich, M., et al. 2002, *Astronomical Society of the Pacific Conference Series*, Vol. 281, *The TERAPIX Pipeline*, 228
- Bertin, E., Schefer, M., Apostolakis, N., et al. 2020, in *Astronomical Society of the Pacific Conference Series*, Vol. 527, *Astronomical Data Analysis Software and Systems XXIX*, ed. R. Pizzo, E. R. Deul, J. D. Mol, J. de Plaa, & H. Verkouter, 461
- Bode, P., Ostriker, J. P., & Turok, N. 2001, *ApJ*, 556, 93
- Brough, S., Collins, C., Demarco, R., et al. 2020, arXiv e-prints, arXiv:2001.11067
- Carlsten, S. G., Greco, J. P., Beaton, R. L., & Greene, J. E. 2020, *ApJ*, 891, 144
- Chambers, K. C., Magnier, E. A., Metcalfe, N., et al. 2016, arXiv e-prints, arXiv:1612.05560
- Cropper, M., Pottinger, S., Niemi, S., et al. 2016, in *Society of Photo-Optical Instrumentation Engineers (SPIE) Conference Series*, Vol. 9904, *Space Telescopes and Instrumentation 2016: Optical, Infrared, and Millimeter Wave*, ed. H. A. MacEwen, G. G. Fazio, M. Lystrup, N. Batalha, N. Siegler, & E. C. Tong, 99040Q

- Cuillandre, J.-C., Bertin, E., Bolzonella, M., et al. 2025a, A&A, 697, A6
- Cuillandre, J.-C., Bolzonella, M., Boselli, A., et al. 2025b, A&A, 697, A11
- Dalcanton, J. J., Williams, B. F., Lang, D., et al. 2012, ApJS, 200, 18
- Dekel, A. & Silk, J. 1986, ApJ, 303, 39
- Dey, A., Schlegel, D. J., Lang, D., et al. 2019, AJ, 157, 168
- Doliva-Dolinsky, A., Martin, N. F., Thomas, G. F., et al. 2022, ApJ, 933, 135
- Doliva-Dolinsky, A., Martin, N. F., Yuan, Z., et al. 2023, ApJ, 952, 72
- Duc, P.-A., Cuillandre, J.-C., Karabal, E., et al. 2015, MNRAS, 446, 120
- Eigenthaler, P., Puzia, T. H., Taylor, M. A., et al. 2018, ApJ, 855, 142
- Euclid Collaboration: Aussel, H., Tereno, I., Schirmer, M., et al. 2025, A&A, submitted (Euclid Q1 SI), arXiv:2503.15302
- Euclid Collaboration: Bellhouse, C., Golden-Marx, J. B., Bamford, S. P., et al. 2025, A&A, in press, <https://doi.org/10.1051/0004-6361/202553887>, arXiv:2503.17455
- Euclid Collaboration: Borlaff, A. S., Gómez-Alvarez, P., Altieri, B., et al. 2022, A&A, 657, A92
- Euclid Collaboration: Cropper, M., Al-Bahlawan, A., Amiaux, J., et al. 2025, A&A, 697, A2
- Euclid Collaboration: Marleau, F. R., Habas, R., Carollo, D., et al. 2025, A&A, submitted (Euclid Q1 SI), arXiv:2503.15335
- Euclid Collaboration: McCracken, H. J., Benson, K., Dolding, C., et al. 2025, A&A, submitted (Euclid Q1 SI), arXiv:2503.15303
- Euclid Collaboration: Mellier, Y., Abdurro'uf, Acevedo Barroso, J., et al. 2025, A&A, 697, A1
- Euclid Collaboration: Polenta, G., Frailis, M., Alavi, A., et al. 2025, A&A, submitted (Euclid Q1 SI), arXiv:2503.15304
- Euclid Collaboration: Romelli, E., Kümmel, M., Dole, H., et al. 2025, A&A, accepted (Euclid Q1 SI), arXiv:2503.15305
- Euclid Collaboration: Scaramella, R., Amiaux, J., Mellier, Y., et al. 2022, A&A, 662, A112
- Euclid Collaboration: Voggel, K., Lançon, A., Saifollahi, T., et al. 2025, A&A, 693, A251
- Ferrarese, L., Côté, P., Cuillandre, J.-C., et al. 2012, ApJS, 200, 4
- Ferrarese, L., Côté, P., MacArthur, L. A., et al. 2020, ApJ, 890, 128
- Forbes, D. A., Ferré-Mateu, A., Durré, M., Brodie, J. P., & Romanowsky, A. J. 2020, MNRAS, 497, 765
- Greco, J. P., Greene, J. E., Strauss, M. A., et al. 2018, ApJ, 857, 104
- Guzmán, R. 2024, in EAS2024, 1990
- Habas, R., Marleau, F. R., Duc, P.-A., et al. 2020, MNRAS, 491, 1901
- Heesters, N., Müller, O., Marleau, F. R., et al. 2023, A&A, 676, A33
- Ibata, R. A., McConnachie, A., Cuillandre, J.-C., et al. 2017, ApJ, 848, 128
- Iodice, E., Cantiello, M., Hilker, M., et al. 2020, A&A, 642, A48
- Ivezić, Ž., Kahn, S. M., Tyson, J. A., et al. 2019, ApJ, 873, 111
- Kaviraj, S., Bichang'a, B., Lazar, I., et al. 2025, MNRAS, 540, 594
- Kelvin, L. S., Hasan, I., & Tyson, J. A. 2023, MNRAS, 520, 2484
- King, I. R. 1966, AJ, 71, 64
- Kluge, M., Hatch, N., Montes, M., et al. 2025, A&A, 697, A13
- Koekemoer, A. & Roman Deep Fields Working Group. 2023, in American Astronomical Society Meeting Abstracts, Vol. 55, American Astronomical Society Meeting Abstracts, 101.02
- Koposov, S. E., Yoo, J., Rix, H.-W., et al. 2009, ApJ, 696, 2179
- Leisman, L., Haynes, M. P., Janowiecki, S., et al. 2017, ApJ, 842, 133
- Lim, S., Côté, P., Peng, E. W., et al. 2020, ApJ, 899, 69
- Marleau, F., Cuillandre, J.-C., Cantiello, M., et al. 2025, A&A, 697, A12
- Marleau, F. R., Habas, R., Poulain, M., et al. 2021, A&A, 654, A105
- McConnachie, A. W. 2012, AJ, 144, 4
- McConnachie, A. W., Irwin, M. J., Ibata, R. A., et al. 2009, Nature, 461, 66
- Merritt, A., van Dokkum, P., Danielli, S., et al. 2016, ApJ, 833, 168
- Müller, O. & Jerjen, H. 2020, A&A, 644, A91
- Nadler, E. O., Mao, Y.-Y., Green, G. M., & Wechsler, R. H. 2019, ApJ, 873, 34
- Nelson, D., Springel, V., Pillepich, A., et al. 2018, Computational Astrophysics and Cosmology, 6, 1
- Ordenes-Briceño, Y., Puzia, T. H., Eigenthaler, P., et al. 2018, ApJ, 860, 4
- Peng, C. Y., Ho, L. C., Impey, C. D., & Rix, H.-W. 2002, AJ, 124, 266
- Poulain, M., Marleau, F. R., Habas, R., et al. 2021, MNRAS, 506, 5494
- Román, J. & Trujillo, I. 2017, MNRAS, 468, 4039
- Rowe, B., Jarvis, M., & Mandelbaum, R. 2014, GalSim: Modular galaxy image simulation toolkit, Astrophysics Source Code Library, record ascl:1402.009
- Saifollahi, T., Lançon, A., Cantiello, M., et al. 2025a, A&A, submitted, arXiv:2503.16367
- Saifollahi, T., Voggel, K., Lançon, A., et al. 2025b, A&A, 697, A10
- Sánchez-Janssen, R., Côté, P., Ferrarese, L., et al. 2019, ApJ, 878, 18
- Sérsic, J. L. 1963, Boletín de la Asociación Argentina de Astronomía La Plata Argentina, 6, 41
- Simon, J. D. 2019, ARA&A, 57, 375
- Spergel, D. N. & Steinhardt, P. J. 2000, Phys. Rev. Lett., 84, 3760
- Teeninga, P., Moschini, U., Trager, S. C., & Wilkinson, M. H. 2015, in International Symposium on Mathematical Morphology and Its Applications to Signal and Image Processing, Springer, 157–168
- Urbano, M., Duc, P. A., Saifollahi, T., et al. 2025, A&A, 700, A104
- Venhola, A., Peletier, R., Laurikainen, E., et al. 2018, A&A, 620, A165
- Venhola, A., Peletier, R., Laurikainen, E., et al. 2017, A&A, 608, A142
- Venhola, A., Peletier, R. F., Salo, H., et al. 2022, A&A, 662, A43
- Watkins, A. E., Kaviraj, S., Collins, C. C., et al. 2024, MNRAS, 528, 4289
- Zaritsky, D., Donnerstein, R., Dey, A., et al. 2019, ApJS, 240, 1
- 1 Université de Strasbourg, CNRS, Observatoire astronomique de Strasbourg, UMR 7550, 67000 Strasbourg, France
 - 2 Space physics and astronomy research unit, University of Oulu, Pentti Kaiteeran katu 1, FI-90014 Oulu, Finland
 - 3 Department of Mathematics and Physics E. De Giorgi, University of Salento, Via per Arnesano, CP-I93, 73100, Lecce, Italy
 - 4 INFN, Sezione di Lecce, Via per Arnesano, CP-193, 73100, Lecce, Italy
 - 5 INAF-Sezione di Lecce, c/o Dipartimento Matematica e Fisica, Via per Arnesano, 73100, Lecce, Italy
 - 6 Universitäts-Sternwarte München, Fakultät für Physik, Ludwig-Maximilians-Universität München, Scheinerstrasse 1, 81679 München, Germany
 - 7 Institut de Física d'Altes Energies (IFAE), The Barcelona Institute of Science and Technology, Campus UAB, 08193 Bellaterra (Barcelona), Spain
 - 8 Institut d'Astrophysique de Paris, UMR 7095, CNRS, and Sorbonne Université, 98 bis boulevard Arago, 75014 Paris, France
 - 9 INAF-Osservatorio Astronomico di Trieste, Via G. B. Tiepolo 11, 34143 Trieste, Italy
 - 10 David A. Dunlap Department of Astronomy & Astrophysics, University of Toronto, 50 St George Street, Toronto, Ontario M5S 3H4, Canada
 - 11 Jodrell Bank Centre for Astrophysics, Department of Physics and Astronomy, University of Manchester, Oxford Road, Manchester M13 9PL, UK
 - 12 Universität Innsbruck, Institut für Astro- und Teilchenphysik, Technikerstr. 25/8, 6020 Innsbruck, Austria
 - 13 Institute of Astronomy, University of Cambridge, Madingley Road, Cambridge CB3 0HA, UK
 - 14 INAF-Osservatorio Astrofisico di Arcetri, Largo E. Fermi 5, 50125, Firenze, Italy
 - 15 Instituto de Astrofísica de Canarias, Vía Láctea, 38205 La Laguna, Tenerife, Spain
 - 16 Universidad de La Laguna, Departamento de Astrofísica, 38206 La Laguna, Tenerife, Spain
 - 17 Sterrenkundig Observatorium, Universiteit Gent, Krijgslaan 281 S9, 9000 Gent, Belgium
 - 18 Departamento de Física Teórica, Atómica y Óptica, Universidad de Valladolid, 47011 Valladolid, Spain
 - 19 Laboratory for Disruptive Interdisciplinary Science (LaDIS), Universidad de Valladolid, 47011 Valladolid, Spain
 - 20 Instituto de Astrofísica e Ciências do Espaço, Faculdade de Ciências, Universidade de Lisboa, Tapada da Ajuda, 1349-018 Lisboa, Portugal
 - 21 INAF - Osservatorio Astronomico d'Abruzzo, Via Maggini, 64100, Teramo, Italy
 - 22 Université Paris-Saclay, Université Paris Cité, CEA, CNRS, AIM, 91191, Gif-sur-Yvette, France
 - 23 Instituto de Física de Cantabria, Edificio Juan Jordá, Avenida de los Castros, 39005 Santander, Spain
 - 24 Max Planck Institute for Extraterrestrial Physics, Giessenbachstr. 1, 85748 Garching, Germany
 - 25 European Southern Observatory, Karl-Schwarzschild-Str. 2, 85748 Garching, Germany
 - 26 INAF-Osservatorio Astronomico di Capodimonte, Via Moirariello 16, 80131 Napoli, Italy
 - 27 Instituto de Astrofísica de Andalucía, CSIC, Glorieta de la Astronomía, 18080, Granada, Spain
 - 28 Institute of Physics, Laboratory of Astrophysics, Ecole Polytechnique Fédérale de Lausanne (EPFL), Observatoire de Sauverny, 1290 Versoix, Switzerland
 - 29 Visiting Fellow, Clare Hall, University of Cambridge, Cambridge, UK

- ³⁰ Instituto de Astrofísica e Ciências do Espaço, Universidade do Porto, CAUP, Rua das Estrelas, PT4150-762 Porto, Portugal
- ³¹ Departamento de Física de la Tierra y Astrofísica, Universidad Complutense de Madrid, Plaza de las Ciencias 2, E-28040 Madrid, Spain
- ³² School of Physics & Astronomy, University of Southampton, Highfield Campus, Southampton SO17 1BJ, UK
- ³³ INAF-Osservatorio Astronomico di Roma, Via Frascati 33, 00078 Monteporzio Catone, Italy
- ³⁴ ESAC/ESA, Camino Bajo del Castillo, s/n., Urb. Villafranca del Castillo, 28692 Villanueva de la Cañada, Madrid, Spain
- ³⁵ Institut für Theoretische Physik, University of Heidelberg, Philosophenweg 16, 69120 Heidelberg, Germany
- ³⁶ INAF-Osservatorio Astronomico di Brera, Via Brera 28, 20122 Milano, Italy
- ³⁷ INAF-Osservatorio di Astrofisica e Scienza dello Spazio di Bologna, Via Piero Gobetti 93/3, 40129 Bologna, Italy
- ³⁸ IFPU, Institute for Fundamental Physics of the Universe, via Beirut 2, 34151 Trieste, Italy
- ³⁹ INFN, Sezione di Trieste, Via Valerio 2, 34127 Trieste TS, Italy
- ⁴⁰ SISSA, International School for Advanced Studies, Via Bonomea 265, 34136 Trieste TS, Italy
- ⁴¹ Dipartimento di Fisica e Astronomia, Università di Bologna, Via Gobetti 93/2, 40129 Bologna, Italy
- ⁴² INFN-Sezione di Bologna, Viale Berti Pichat 6/2, 40127 Bologna, Italy
- ⁴³ Dipartimento di Fisica, Università di Genova, Via Dodecaneso 33, 16146, Genova, Italy
- ⁴⁴ INFN-Sezione di Genova, Via Dodecaneso 33, 16146, Genova, Italy
- ⁴⁵ Department of Physics "E. Pancini", University Federico II, Via Cinthia 6, 80126, Napoli, Italy
- ⁴⁶ Dipartimento di Fisica, Università degli Studi di Torino, Via P. Giuria 1, 10125 Torino, Italy
- ⁴⁷ INFN-Sezione di Torino, Via P. Giuria 1, 10125 Torino, Italy
- ⁴⁸ INAF-Osservatorio Astrofisico di Torino, Via Osservatorio 20, 10025 Pino Torinese (TO), Italy
- ⁴⁹ European Space Agency/ESTEC, Keplerlaan 1, 2201 AZ Noordwijk, The Netherlands
- ⁵⁰ Leiden Observatory, Leiden University, Einsteinweg 55, 2333 CC Leiden, The Netherlands
- ⁵¹ INAF-IASF Milano, Via Alfonso Corti 12, 20133 Milano, Italy
- ⁵² Centro de Investigaciones Energéticas, Medioambientales y Tecnológicas (CIEMAT), Avenida Complutense 40, 28040 Madrid, Spain
- ⁵³ Port d'Informació Científica, Campus UAB, C. Albareda s/n, 08193 Bellaterra (Barcelona), Spain
- ⁵⁴ Institute for Theoretical Particle Physics and Cosmology (TTK), RWTH Aachen University, 52056 Aachen, Germany
- ⁵⁵ INFN section of Naples, Via Cinthia 6, 80126, Napoli, Italy
- ⁵⁶ Dipartimento di Fisica e Astronomia "Augusto Righi" - Alma Mater Studiorum Università di Bologna, Viale Berti Pichat 6/2, 40127 Bologna, Italy
- ⁵⁷ Institute for Astronomy, University of Edinburgh, Royal Observatory, Blackford Hill, Edinburgh EH9 3HJ, UK
- ⁵⁸ European Space Agency/ESRIN, Largo Galileo Galilei 1, 00044 Frascati, Roma, Italy
- ⁵⁹ Université Claude Bernard Lyon 1, CNRS/IN2P3, IP2I Lyon, UMR 5822, Villeurbanne, F-69100, France
- ⁶⁰ Institut de Ciències del Cosmos (ICCUB), Universitat de Barcelona (IEEC-UB), Martí i Franquès 1, 08028 Barcelona, Spain
- ⁶¹ Institució Catalana de Recerca i Estudis Avançats (ICREA), Passeig de Lluís Companys 23, 08010 Barcelona, Spain
- ⁶² UCB Lyon 1, CNRS/IN2P3, IUF, IP2I Lyon, 4 rue Enrico Fermi, 69622 Villeurbanne, France
- ⁶³ Mullard Space Science Laboratory, University College London, Holmbury St Mary, Dorking, Surrey RH5 6NT, UK
- ⁶⁴ Departamento de Física, Faculdade de Ciências, Universidade de Lisboa, Edifício C8, Campo Grande, PT1749-016 Lisboa, Portugal
- ⁶⁵ Instituto de Astrofísica e Ciências do Espaço, Faculdade de Ciências, Universidade de Lisboa, Campo Grande, 1749-016 Lisboa, Portugal
- ⁶⁶ Department of Astronomy, University of Geneva, ch. d'Ecogia 16, 1290 Versoix, Switzerland
- ⁶⁷ Université Paris-Saclay, CNRS, Institut d'astrophysique spatiale, 91405, Orsay, France
- ⁶⁸ INFN-Padova, Via Marzolo 8, 35131 Padova, Italy
- ⁶⁹ Aix-Marseille Université, CNRS/IN2P3, CPPM, Marseille, France
- ⁷⁰ INAF-Istituto di Astrofisica e Planetologia Spaziali, via del Fosso del Cavaliere, 100, 00100 Roma, Italy
- ⁷¹ INFN-Bologna, Via Irnerio 46, 40126 Bologna, Italy
- ⁷² University Observatory, LMU Faculty of Physics, Scheinerstrasse 1, 81679 Munich, Germany
- ⁷³ INAF-Osservatorio Astronomico di Padova, Via dell'Osservatorio 5, 35122 Padova, Italy
- ⁷⁴ Dipartimento di Fisica "Aldo Pontremoli", Università degli Studi di Milano, Via Celoria 16, 20133 Milano, Italy
- ⁷⁵ INFN-Sezione di Milano, Via Celoria 16, 20133 Milano, Italy
- ⁷⁶ Institute of Theoretical Astrophysics, University of Oslo, P.O. Box 1029 Blindern, 0315 Oslo, Norway
- ⁷⁷ Jet Propulsion Laboratory, California Institute of Technology, 4800 Oak Grove Drive, Pasadena, CA, 91109, USA
- ⁷⁸ Department of Physics, Lancaster University, Lancaster, LA1 4YB, UK
- ⁷⁹ Felix Hormuth Engineering, Goethestr. 17, 69181 Leimen, Germany
- ⁸⁰ Technical University of Denmark, Elektrovej 327, 2800 Kgs. Lynby, Denmark
- ⁸¹ Cosmic Dawn Center (DAWN), Denmark
- ⁸² Max-Planck-Institut für Astronomie, Königstuhl 17, 69117 Heidelberg, Germany
- ⁸³ NASA Goddard Space Flight Center, Greenbelt, MD 20771, USA
- ⁸⁴ Department of Physics and Astronomy, University College London, Gower Street, London WC1E 6BT, UK
- ⁸⁵ Department of Physics and Helsinki Institute of Physics, Gustaf Hållströmin katu 2, University of Helsinki, 00014 Helsinki, Finland
- ⁸⁶ Université de Genève, Département de Physique Théorique and Centre for Astroparticle Physics, 24 quai Ernest-Ansermet, CH-1211 Genève 4, Switzerland
- ⁸⁷ Department of Physics, P.O. Box 64, University of Helsinki, 00014 Helsinki, Finland
- ⁸⁸ Helsinki Institute of Physics, Gustaf Hållströmin katu 2, University of Helsinki, 00014 Helsinki, Finland
- ⁸⁹ Kapteyn Astronomical Institute, University of Groningen, PO Box 800, 9700 AV Groningen, The Netherlands
- ⁹⁰ Laboratoire d'étude de l'Univers et des phénomènes eXtremes, Observatoire de Paris, Université PSL, Sorbonne Université, CNRS, 92190 Meudon, France
- ⁹¹ SKAO, Jodrell Bank, Lower Withington, Macclesfield SK11 9FT, United Kingdom
- ⁹² Centre de Calcul de l'IN2P3/CNRS, 21 avenue Pierre de Coubertin 69627 Villeurbanne Cedex, France
- ⁹³ Universität Bonn, Argelander-Institut für Astronomie, Auf dem Hügel 71, 53121 Bonn, Germany
- ⁹⁴ INFN-Sezione di Roma, Piazzale Aldo Moro, 2 - c/o Dipartimento di Fisica, Edificio G. Marconi, 00185 Roma, Italy
- ⁹⁵ Aix-Marseille Université, CNRS, CNES, LAM, Marseille, France
- ⁹⁶ Dipartimento di Fisica e Astronomia "Augusto Righi" - Alma Mater Studiorum Università di Bologna, via Piero Gobetti 93/2, 40129 Bologna, Italy
- ⁹⁷ Department of Physics, Institute for Computational Cosmology, Durham University, South Road, Durham, DH1 3LE, UK
- ⁹⁸ Université Paris Cité, CNRS, Astroparticule et Cosmologie, 75013 Paris, France
- ⁹⁹ CNRS-UCB International Research Laboratory, Centre Pierre Binétruy, IRL2007, CPB-IN2P3, Berkeley, USA
- ¹⁰⁰ Institut d'Astrophysique de Paris, 98bis Boulevard Arago, 75014, Paris, France

- 101 Telespazio UK S.L. for European Space Agency (ESA), Camino bajo del Castillo, s/n, Urbanizacion Villafranca del Castillo, Villanueva de la Cañada, 28692 Madrid, Spain
- 102 DARK, Niels Bohr Institute, University of Copenhagen, Jagtvej 155, 2200 Copenhagen, Denmark
- 103 Space Science Data Center, Italian Space Agency, via del Politecnico snc, 00133 Roma, Italy
- 104 Centre National d'Etudes Spatiales – Centre spatial de Toulouse, 18 avenue Edouard Belin, 31401 Toulouse Cedex 9, France
- 105 Institute of Space Science, Str. Atomistilor, nr. 409 Măgurele, Ilfov, 077125, Romania
- 106 Consejo Superior de Investigaciones Científicas, Calle Serrano 117, 28006 Madrid, Spain
- 107 Dipartimento di Fisica e Astronomia "G. Galilei", Università di Padova, Via Marzolo 8, 35131 Padova, Italy
- 108 Institut de Recherche en Astrophysique et Planétologie (IRAP), Université de Toulouse, CNRS, UPS, CNES, 14 Av. Edouard Belin, 31400 Toulouse, France
- 109 Université St Joseph; Faculty of Sciences, Beirut, Lebanon
- 110 Departamento de Física, FCFM, Universidad de Chile, Blanco Encalada 2008, Santiago, Chile
- 111 Institut d'Estudis Espacials de Catalunya (IEEC), Edifici RDIT, Campus UPC, 08860 Castelldefels, Barcelona, Spain
- 112 Satlantis, University Science Park, Sede Bld 48940, Leioa-Bilbao, Spain
- 113 Institute of Space Sciences (ICE, CSIC), Campus UAB, Carrer de Can Magrans, s/n, 08193 Barcelona, Spain
- 114 Infrared Processing and Analysis Center, California Institute of Technology, Pasadena, CA 91125, USA
- 115 Cosmic Dawn Center (DAWN)
- 116 Niels Bohr Institute, University of Copenhagen, Jagtvej 128, 2200 Copenhagen, Denmark
- 117 Universidad Politécnica de Cartagena, Departamento de Electrónica y Tecnología de Computadoras, Plaza del Hospital 1, 30202 Cartagena, Spain
- 118 Astronomisches Rechen-Institut, Zentrum für Astronomie der Universität Heidelberg, Mönchhofstr. 12-14, 69120 Heidelberg, Germany
- 119 Dipartimento di Fisica e Scienze della Terra, Università degli Studi di Ferrara, Via Giuseppe Saragat 1, 44122 Ferrara, Italy
- 120 Istituto Nazionale di Fisica Nucleare, Sezione di Ferrara, Via Giuseppe Saragat 1, 44122 Ferrara, Italy
- 121 INAF, Istituto di Radioastronomia, Via Piero Gobetti 101, 40129 Bologna, Italy
- 122 Université Côte d'Azur, Observatoire de la Côte d'Azur, CNRS, Laboratoire Lagrange, Bd de l'Observatoire, CS 34229, 06304 Nice cedex 4, France
- 123 Department of Physics, Oxford University, Keble Road, Oxford OX1 3RH, UK
- 124 Instituto de Astrofísica de Canarias (IAC); Departamento de Astrofísica, Universidad de La Laguna (ULL), 38200, La Laguna, Tenerife, Spain
- 125 Université PSL, Observatoire de Paris, Sorbonne Université, CNRS, LERMA, 75014, Paris, France
- 126 Université Paris-Cité, 5 Rue Thomas Mann, 75013, Paris, France
- 127 Aurora Technology for European Space Agency (ESA), Camino bajo del Castillo, s/n, Urbanizacion Villafranca del Castillo, Villanueva de la Cañada, 28692 Madrid, Spain
- 128 ICL, Junia, Université Catholique de Lille, LITL, 59000 Lille, France
- 129 ICSC - Centro Nazionale di Ricerca in High Performance Computing, Big Data e Quantum Computing, Via Magnanelli 2, Bologna, Italy
- 130 Instituto de Física Teórica UAM-CSIC, Campus de Cantoblanco, 28049 Madrid, Spain
- 131 CERCA/ISO, Department of Physics, Case Western Reserve University, 10900 Euclid Avenue, Cleveland, OH 44106, USA
- 132 Technical University of Munich, TUM School of Natural Sciences, Physics Department, James-Frank-Str. 1, 85748 Garching, Germany
- 133 Max-Planck-Institut für Astrophysik, Karl-Schwarzschild-Str. 1, 85748 Garching, Germany
- 134 Laboratoire Univers et Théorie, Observatoire de Paris, Université PSL, Université Paris Cité, CNRS, 92190 Meudon, France
- 135 Departamento de Física Fundamental. Universidad de Salamanca. Plaza de la Merced s/n. 37008 Salamanca, Spain
- 136 Center for Data-Driven Discovery, Kavli IPMU (WPI), UTIAS, The University of Tokyo, Kashiwa, Chiba 277-8583, Japan
- 137 Waterloo Centre for Astrophysics, University of Waterloo, Waterloo, Ontario N2L 3G1, Canada
- 138 Dipartimento di Fisica - Sezione di Astronomia, Università di Trieste, Via Tiepolo 11, 34131 Trieste, Italy
- 139 California Institute of Technology, 1200 E California Blvd, Pasadena, CA 91125, USA
- 140 Department of Physics & Astronomy, University of California Irvine, Irvine CA 92697, USA
- 141 Departamento Física Aplicada, Universidad Politécnica de Cartagena, Campus Muralla del Mar, 30202 Cartagena, Murcia, Spain
- 142 CEA Saclay, DFR/IRFU, Service d'Astrophysique, Bat. 709, 91191 Gif-sur-Yvette, France
- 143 Institute of Cosmology and Gravitation, University of Portsmouth, Portsmouth PO1 3FX, UK
- 144 Department of Computer Science, Aalto University, PO Box 15400, Espoo, FI-00076, Finland
- 145 Instituto de Astrofísica de Canarias, c/ Via Lactea s/n, La Laguna 38200, Spain. Departamento de Astrofísica de la Universidad de La Laguna, Avda. Francisco Sanchez, La Laguna, 38200, Spain
- 146 Ruhr University Bochum, Faculty of Physics and Astronomy, Astronomical Institute (AIRUB), German Centre for Cosmological Lensing (GCCL), 44780 Bochum, Germany
- 147 Department of Physics and Astronomy, Vesilinnantie 5, University of Turku, 20014 Turku, Finland
- 148 Serco for European Space Agency (ESA), Camino bajo del Castillo, s/n, Urbanizacion Villafranca del Castillo, Villanueva de la Cañada, 28692 Madrid, Spain
- 149 ARC Centre of Excellence for Dark Matter Particle Physics, Melbourne, Australia
- 150 Centre for Astrophysics & Supercomputing, Swinburne University of Technology, Hawthorn, Victoria 3122, Australia
- 151 Department of Physics and Astronomy, University of the Western Cape, Bellville, Cape Town, 7535, South Africa
- 152 DAMTP, Centre for Mathematical Sciences, Wilberforce Road, Cambridge CB3 0WA, UK
- 153 Kavli Institute for Cosmology Cambridge, Madingley Road, Cambridge, CB3 0HA, UK
- 154 Department of Astrophysics, University of Zurich, Winterthurerstrasse 190, 8057 Zurich, Switzerland
- 155 Department of Physics, Centre for Extragalactic Astronomy, Durham University, South Road, Durham, DH1 3LE, UK
- 156 IRFU, CEA, Université Paris-Saclay 91191 Gif-sur-Yvette Cedex, France
- 157 Oskar Klein Centre for Cosmoparticle Physics, Department of Physics, Stockholm University, Stockholm, SE-106 91, Sweden
- 158 Astrophysics Group, Blackett Laboratory, Imperial College London, London SW7 2AZ, UK
- 159 Univ. Grenoble Alpes, CNRS, Grenoble INP, LPSC-IN2P3, 53, Avenue des Martyrs, 38000, Grenoble, France
- 160 Dipartimento di Fisica, Sapienza Università di Roma, Piazzale Aldo Moro 2, 00185 Roma, Italy
- 161 Centro de Astrofísica da Universidade do Porto, Rua das Estrelas, 4150-762 Porto, Portugal
- 162 HE Space for European Space Agency (ESA), Camino bajo del Castillo, s/n, Urbanizacion Villafranca del Castillo, Villanueva de la Cañada, 28692 Madrid, Spain
- 163 Theoretical astrophysics, Department of Physics and Astronomy, Uppsala University, Box 516, 751 37 Uppsala, Sweden
- 164 Institute for Astronomy, University of Hawaii, 2680 Woodlawn Drive, Honolulu, HI 96822, USA
- 165 Mathematical Institute, University of Leiden, Einsteinweg 55, 2333 CA Leiden, The Netherlands

¹⁶⁶ Univ. Lille, CNRS, Centrale Lille, UMR 9189 CRIStAL, 59000 Lille, France

¹⁶⁷ Department of Astrophysical Sciences, Peyton Hall, Princeton University, Princeton, NJ 08544, USA

¹⁶⁸ Center for Computational Astrophysics, Flatiron Institute, 162 5th Avenue, 10010, New York, NY, USA

Appendix A: MER mosaic

The MER VIS mosaic used for this work is shown in Fig. A.1.

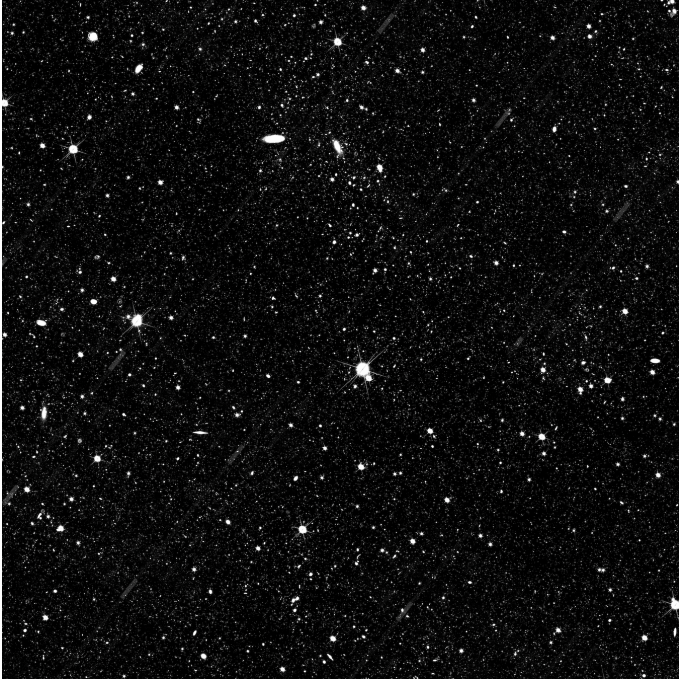


Fig. A.1: The chosen MER VIS mosaic. The tile with ID 102018187 is centred on RA = $2^{\circ} 35' 43''.41$, Dec = $-51^{\circ} 30' 0''.00$. Its x - and y -axes correspond to RA and Dec, respectively. Its side length is $32'$ (for a description of the tiling scheme see [Euclid Collaboration: Romelli et al. 2025](#)). Data from this tile will be publicly available as part of the *Euclid* first data release (DR1).

Appendix B: Crossmatch search radius

In this appendix, we discuss briefly the definition of our search radius R_{SEARCH} , used for the crossmatch between the input parameter catalogue of injected mock dwarfs, and the final MER catalogue.

While standard crossmatch procedures use a fixed radius, we opted instead for a radius that varies depending on the galaxy being searched for. Specifically, for each dwarf in the input catalogue, we perform a search in the final MER catalogue within a R_{SEARCH} centred on its input position, R_{SEARCH} depending on the input size of the galaxy. We use the full input R_e when it is unaffected by the MER background subtraction (i.e., for $R_{\text{SEARCH}} < 10''$), and $R_e/2$ in all other cases.

Our tests also included other R_{SEARCH} definitions, such as the theoretical $25 \text{ mag arcsec}^{-2}$ isophotal radius, which on average matched the size of the MER segmentation masks better than the effective radius, but was not defined for galaxies fainter than this surface brightness. Except for those faint galaxies, the results did not vary with the final definition adopted for R_{SEARCH} .

Appendix C: Detectability as a function of $\langle\mu_i\rangle$

[Euclid Collaboration: Marleau et al. \(2025\)](#) uses $\langle\mu_i\rangle$, defined as the average surface brightness computed with the columns FLUX_SEGMENTATION and SEGMENTATION_AREA of the final MER catalogues. We thus provide below Fig. C.1, which is a version of the Fig. 4 using this metrics. Please note that the relation between the input SB_e of injected galaxies and the MER output $\langle\mu_i\rangle$ is extrapolated for the dwarfs not detected by MER.

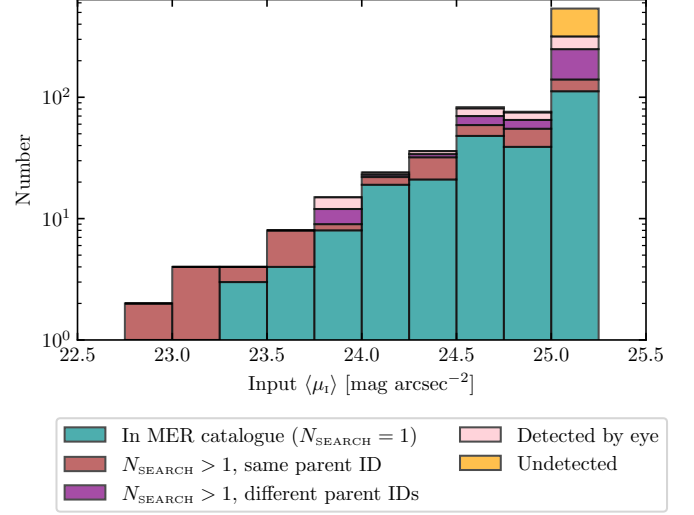


Fig. C.1: Histograms of the input $\langle\mu_i\rangle$, colour-coded according to their detection by eye and in the MER catalogue, with N_{SEARCH} the number of MER sources found in the search radius R_{SEARCH} used for the crossmatch.

Appendix D: Non-corrected detectability

The complete results for the dwarf detectability before the contaminant correction are given in Fig. D.1 and in Tables D.1 and D.2. Those values represent upper limits. It is worth noting that in the main body of the paper, the values given take into account the single parent ID detections.

Appendix E: Distance and dwarf detectability

We provide further detail on the impact of the distance on the dwarf detectability in Fig. E.1 and the associated Tables E.1 and E.2.

Appendix F: Details on the visual inspection

Here, we detail the results of our visual inspection in each dwarf cutout for the three types of image (NOBG, VIS BGSUB, and final MER mosaics). The motivations for this study are the following.

- To identify and exclude cases where source matching between the input dwarf catalogue and the final MER catalogue is unreliable due to contamination or confusion with background objects. Such cases are removed from the corrected detection statistics discussed in the main text. The results before that correction are available in Appendix D.
- Evaluating the impact of the background subtraction on the detection of dwarf galaxies, with or without a nuclear star cluster. We detail below the results of this study.

Table D.1: Comparison between the detection statistics across different SB_e bins. Column (1) gives the SB_e bin in mag arcsec^{-2} . Columns (2) indicates the number of injected dwarfs. The remaining columns are the number of dwarfs that are (3) present in the final MER catalogue as one single object, (4) present in the final MER catalogue as one or several objects sharing the same parent ID. Column (4) includes the detections from Column (3). They are given in number and in percent of the injected dwarfs in the corresponding surface brightness bin.

| SB_e | Input dwarfs | In MER catalogue | Single parent ID |
|--------|--------------|------------------|------------------|
| (1) | (2) | (3) | (4) |
| 21–22 | 6 (100 %) | 2 (33 %) | 6 (100 %) |
| 22–23 | 18 (100 %) | 8 (44 %) | 14 (78 %) |
| 23–24 | 68 (100 %) | 51 (75 %) | 64 (94 %) |
| 24–25 | 192 (100 %) | 123 (64 %) | 154 (80 %) |
| 25–26 | 202 (100 %) | 104 (51 %) | 114 (56 %) |
| 26–27 | 173 (100 %) | 28 (16 %) | 54 (31 %) |
| 27–28 | 101 (100 %) | 17 (17 %) | 38 (38 %) |
| 28–29 | 11 (100 %) | 3 (27 %) | 7 (63 %) |
| 29–30 | 16 (100 %) | 4 (25 %) | 8 (50 %) |
| 30–31 | 4 (100 %) | 1 (25 %) | 1 (25 %) |

Table D.2: Similar to Table D.1, but now binning the data in R_e instead of in SB_e .

| R_e [arcsec] | Input dwarfs | In MER catalogue | Single parent ID |
|----------------|--------------|------------------|------------------|
| (1) | (2) | (3) | (4) |
| 0–2.5 | 317 (100 %) | 120 (38 %) | 146 (46 %) |
| 2.5–5 | 201 (100 %) | 95 (47 %) | 134 (67 %) |
| 5–7.5 | 130 (100 %) | 59 (45 %) | 91 (70 %) |
| 7.5–10 | 46 (100 %) | 22 (48 %) | 31 (67 %) |
| 10–12.5 | 39 (100 %) | 19 (49 %) | 23 (59 %) |
| 12.5–15 | 15 (100 %) | 10 (67 %) | 11 (73 %) |
| 15–17.5 | 17 (100 %) | 8 (47 %) | 11 (65 %) |
| 17.5–20 | 8 (100 %) | 4 (50 %) | 6 (75 %) |
| 20–22.5 | 5 (100 %) | 1 (20 %) | 1 (20 %) |
| 22.5–25 | 10 (100 %) | 2 (20 %) | 5 (50 %) |
| 25–27.5 | 3 (100 %) | 0 (0 %) | 1 (33 %) |
| 37.5–40 | 1 (100 %) | 1 (100 %) | 1 (100 %) |
| 40–42.5 | 2 (100 %) | 2 (100 %) | 2 (100 %) |

Figure F.1 compiles the results of the visual detection for galaxies at all distances and demonstrates the visual detectability of each dwarf according to their input parameters. Nucleated dwarfs were excluded from this test, to ensure that we are not impacted by the detectability of the nucleus alone. The left panel includes parameter space plots (the input R_e as a function of the input I_e) which are colour-coded according to the visual detectability of the dwarf for the three types of products (NOBG,

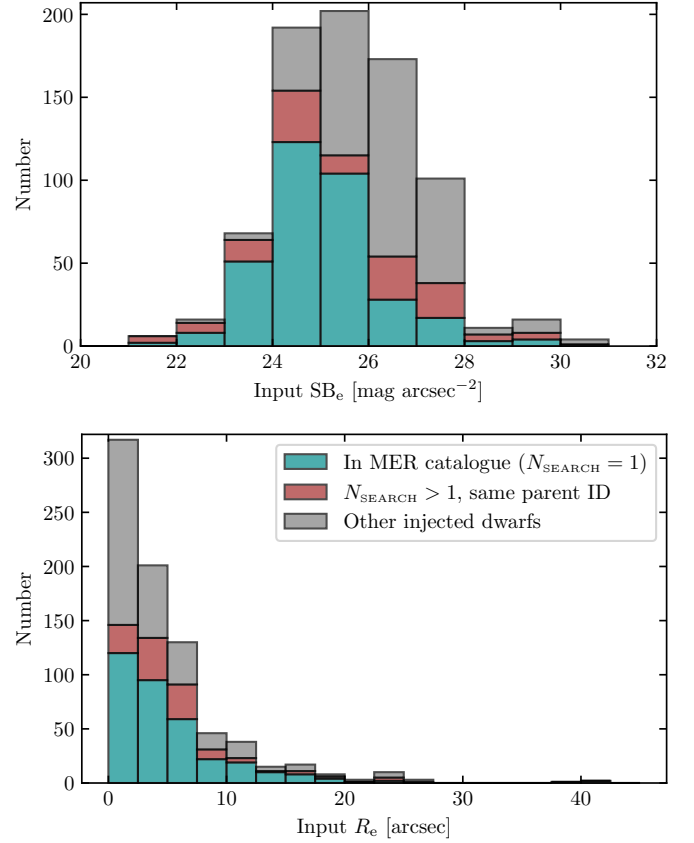


Fig. D.1: Histograms of the input SB_e (top panel) and the input R_e (bottom panel), colour-coded according to their detection by eye and in the MER catalogue, N_{SEARCH} being the number of MER sources found by using the search radius R_{SEARCH} for the crossmatch.

VIS BGSUB, and final MER mosaics). We then construct the right panel of Fig. F.1, i.e. the histograms of SB_e for the three products, using the detection information already employed in the previous plot.

Finally, we repeat the above analysis for the nucleated dwarfs, as shown in Fig. F.2. When we compare with Fig. F.1, we note that the presence of a nucleus has a slight impact on dwarf detection, but does not significantly alter the distribution within the parameter space or the SB_e histogram. For a few faint dwarfs, it seems to facilitate their identification (examples are provided in the highlighted region of the left panel, where some nucleated dwarfs remain detected after the background subtraction whereas the non-nucleated dwarfs are not). This is the reason why fewer dwarfs are lost among the background subtractions in the case of nucleated dwarfs (5 lost with $26 \text{ mag arcsec}^{-2} < SB_e < 28 \text{ mag arcsec}^{-2}$, compared to 8 for non-nucleated dwarfs).

We are now interested in the impact of the background subtractions. We first focus on comparing the rows of Figs. F.1 and F.2 that pertain to the final MER mosaic and the VIS BGSUB mosaic, in order to probe the effect of the second, local, MER background subtraction. It has very little impact on the parameter space plot and on the global shape of the SB_e histogram. Between the two background subtractions, only a small number (14, or 2 %) of the injected dwarfs, highlighted in the dashed box in the parameter space plots, are lost above $SB_e = 24 \text{ mag arcsec}^{-2}$, showing that the subtraction slightly affects only the LSB regime, while remarkably preserving the vast majority of detectable dwarfs.

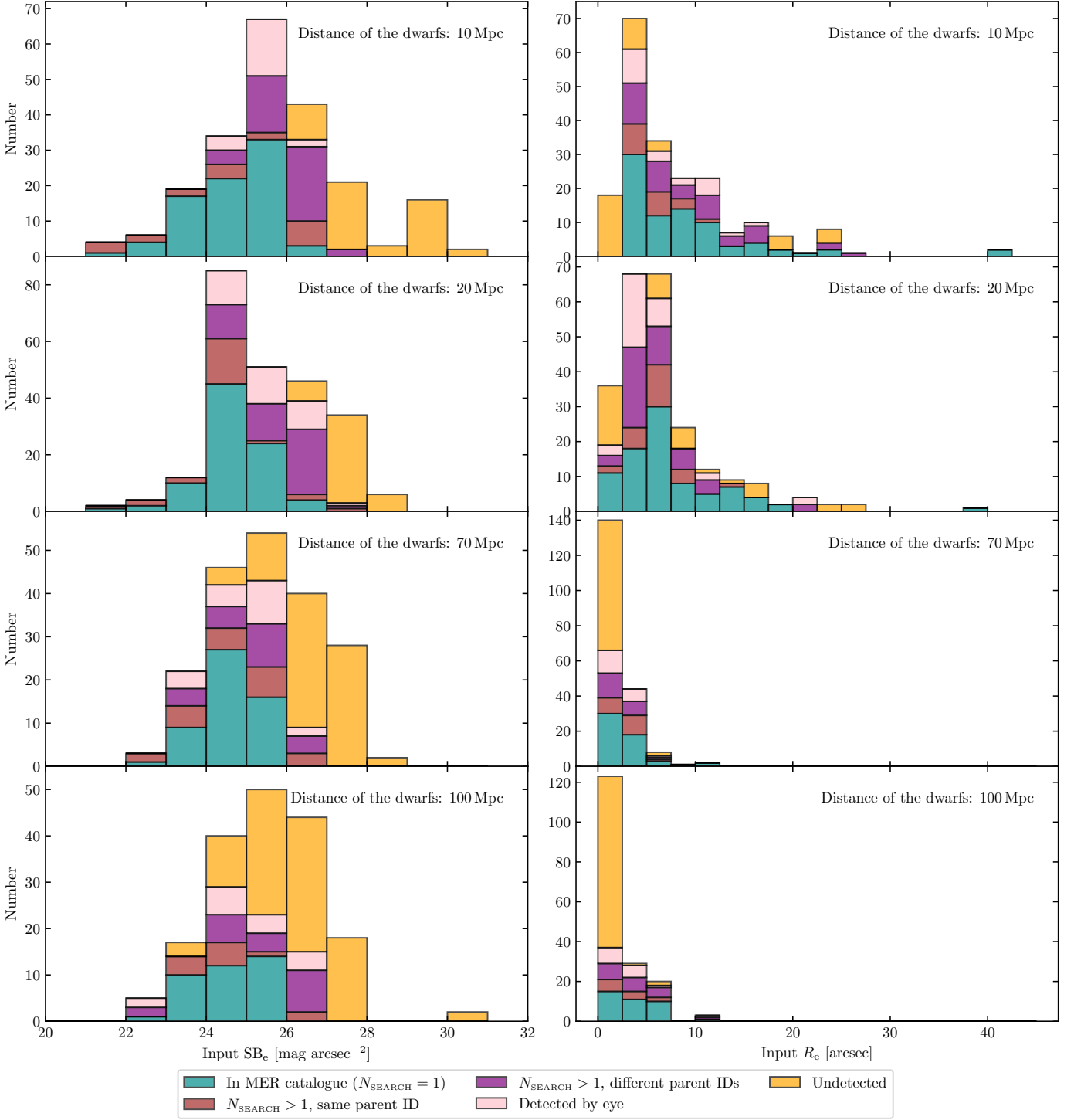


Fig. E.1: Histograms of the input SB_e (left panel) and the input R_e (right panel) of the dwarfs at 10, 20, 70 and 100 Mpc, colour-coded according to their detection by eye and in the MER catalogue, with N_{SEARCH} the number of MER sources found in the search radius R_{SEARCH} used for the crossmatch.

We then focus on comparing the first and second rows of Figs. F.1 and F.2 that pertain to the VIS BGSUB and NOBG mosaics, in order to probe the effect of the first VIS background subtraction. Our conclusions on the dwarf detectability are similar to those reported for the MER second local background subtraction, i.e. we observe very little impact on dwarf detection rates, losing a very small number of dwarfs above $SB_e = 24 \text{ mag arcsec}^{-2}$ (7 dwarfs or 1 % of the injected dwarfs).

Table E.1: Representative detection statistics for the sample. For each distance D (column 1, given in Mpc), we extract the SB_e bin with the highest number of dwarfs (column 2, given in mag arcsec^{-2}). Column (3) indicates the number of injected dwarfs. The remaining columns are the number of dwarfs that are (4) present in the final MER catalogue as one single object, (5) present in the final MER catalogue as one or several objects sharing the same parent ID, (6) present in the final MER catalogue as one or several objects sharing or not the same parent ID(s), and (7) visually detected, whether or not they are present in the final MER catalogue. As a result, columns (4) to (6) are cumulative. Columns (3) to (7) are given in number and in percent of the injected dwarfs in the corresponding surface brightness bin.

| D [Mpc] | SB_e [mag arcsec^{-2}] | Input dwarfs | In MER catalogue | Single parent ID | Single or multiple parent ID(s) | Detected by eye |
|-----------|-------------------------------------|--------------|------------------|------------------|---------------------------------|-----------------|
| (1) | (2) | (3) | (4) | (5) | (6) | (7) |
| 10 | 25–26 | 67 (100 %) | 33 (49 %) | 35 (52 %) | 51 (76 %) | 67 (100 %) |
| 20 | 24–25 | 85 (100 %) | 45 (53 %) | 61 (72 %) | 73 (86 %) | 85 (100 %) |
| 70 | 25–26 | 54 (100 %) | 16 (30 %) | 23 (43 %) | 33 (61 %) | 43 (80 %) |
| 100 | 25–26 | 50 (100 %) | 14 (28 %) | 15 (30 %) | 19 (38 %) | 23 (46 %) |

Table E.2: Similar to Table E.1, but with bins in R_e (in arcsec) rather than in SB_e .

| D | R_e bin | Input dwarfs | In MER catalogue | Single parent ID | Single or multiple parent ID(s) | Detected by eye |
|-----|-----------|--------------|------------------|------------------|---------------------------------|-----------------|
| (1) | (2) | (3) | (4) | (5) | (6) | (7) |
| 10 | 2.5–5 | 70 (100 %) | 30 (43 %) | 39 (56 %) | 51 (73 %) | 61 (87 %) |
| 20 | 2.5–7.5 | 136 (100 %) | 48 (35 %) | 66 (49 %) | 100 (74 %) | 129 (95 %) |
| 70 | 0–2.5 | 140 (100 %) | 30 (21 %) | 39 (28 %) | 53 (38 %) | 66 (47 %) |
| 100 | 0–2.5 | 123 (100 %) | 15 (12 %) | 21 (17 %) | 29 (24 %) | 37 (30 %) |

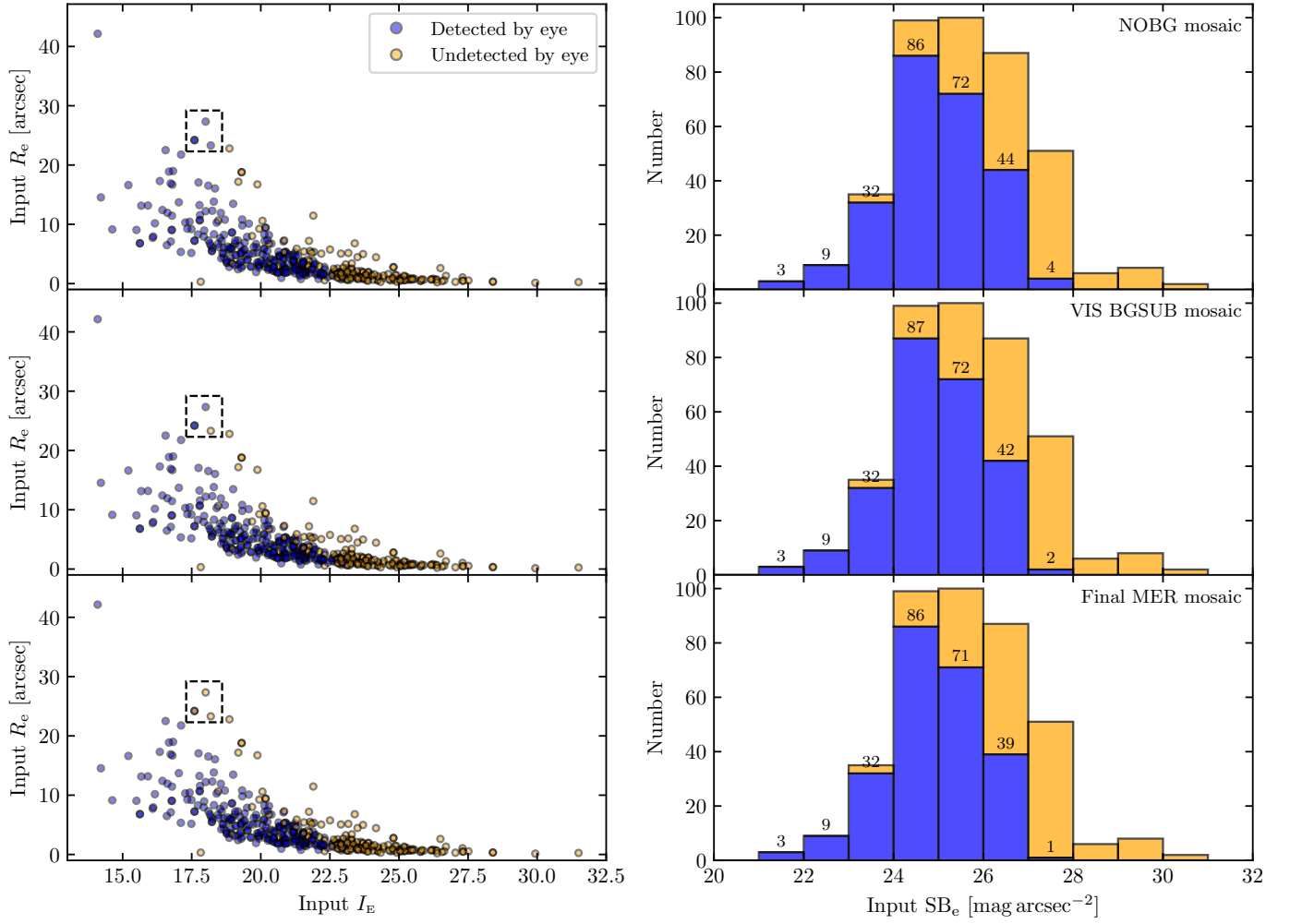


Fig. F.1: Input R_e as a function of the input total magnitude in I_E (left panel) and the corresponding histogram of the input SB_e (right panel), colour-coded according to their detection or non-detection by eye in the three types of products: NOBG, VIS BGSUB, and the final MER mosaic subtracted by VIS and MER backgrounds. Only the non-nucleated dwarfs, at all distances, have been used in this analysis. We labelled the number of dwarfs that are visually detected in each SB_e bin. The dashed rectangle shows examples of objects that were detected differently with the various background treatments.

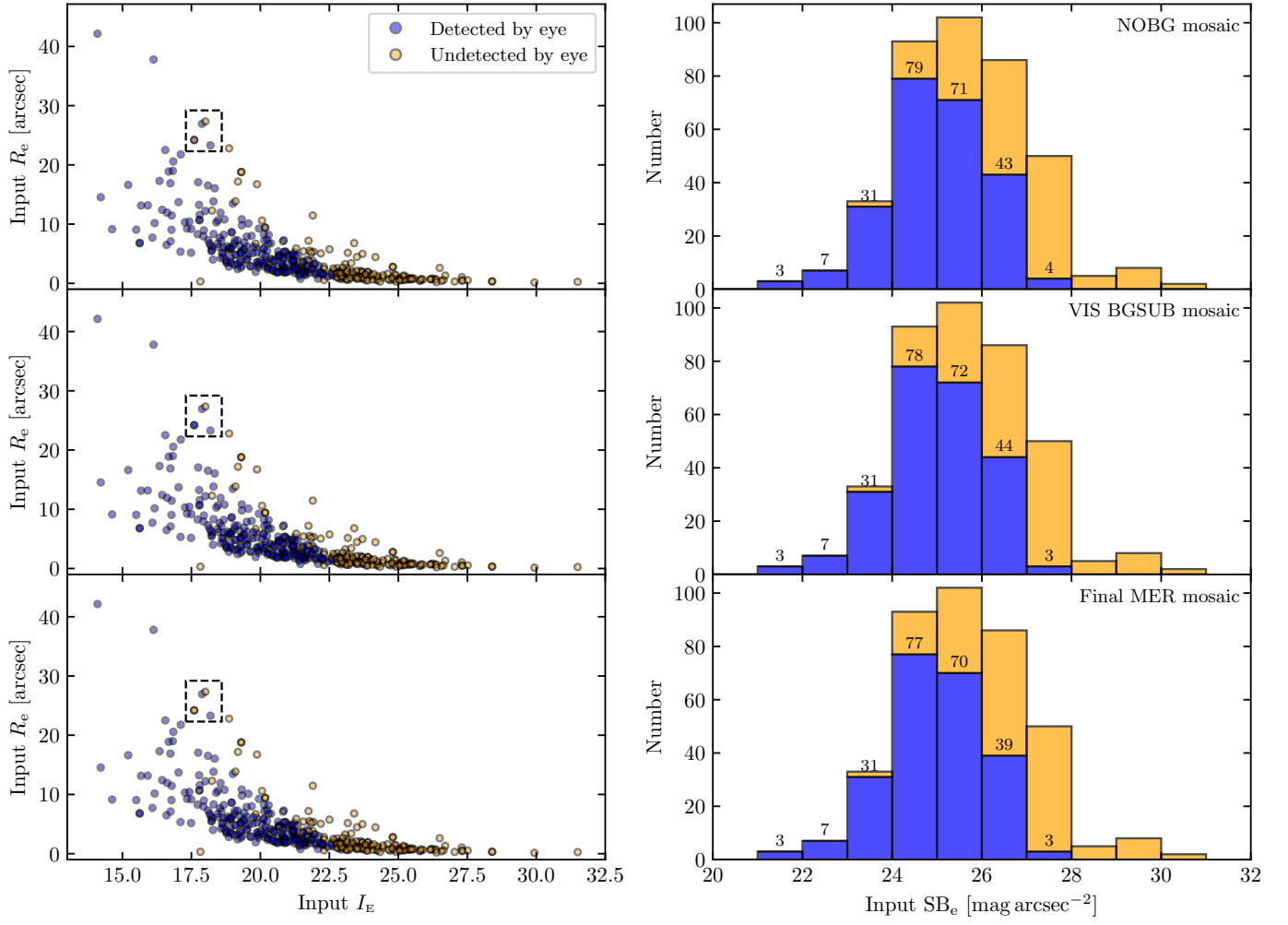


Fig. F.2: Identical to Fig. F.1, but for nucleated dwarf galaxies.